


 CrossMark
 click for updates

 Cite this: *J. Anal. At. Spectrom.*, 2016,
 31, 2305

Influence of laser parameters on isotope fractionation and optimisation of lithium and boron isotope ratio measurements using laser ablation-multiple Faraday collector-inductively coupled plasma mass spectrometry†

 Jun-Ichi Kimura,^{*a} Qing Chang,^a Tsuyoshi Ishikawa^b and Tatsuki Tsujimori^c

We report the origin of isotope fractionation induced by the choice of laser parameters and a method for accurate *in situ* determination of lithium ($\delta^7\text{Li}$) and boron ($\delta^{11}\text{B}$) isotope ratios in glasses and minerals using laser ablation multiple Faraday collector inductively coupled plasma mass spectrometry (LA-MFC-ICPMS). Laser ablation parameters were examined using 266 nm femtosecond (266FsLA) and 193 nm nanosecond excimer (193ExLA) laser ablation systems for crater diameters of 30–200 μm . We found that higher laser repetition rates and larger crater diameters have led to enhanced fractionation of lighter isotopes, as much as -8‰ for both $\delta^7\text{Li}$ and $\delta^{11}\text{B}$. Fractionation was primarily affected by the ICP aerosol loading and secondly by the thermal fractionation at the LA site. The former was accounted for by mass loading effects, which lowered the plasma temperature and led to insufficient aerosol vaporisation. The latter was related to the molten layer on the crater walls, which resulted in coarser and heavier $\delta^7\text{Li}$ and $\delta^{11}\text{B}$ aerosols that did not reach the ICP. Both processes can result in Rayleigh fractionation during aerosol formation and vaporisation. Controlled ablation using a constant crater size, repetition rate, and high laser fluence of 193ExLA enabled reproducible ablation for the standard NIST SRM 61X glasses and unknown basalt glasses. Based on the principles of isotopic fractionation deduced from our experiments, we propose a novel ablation volume correction (AVC) protocol for accurate isotopic analyses of various samples with different matrices. Both the repeatability and the laboratory bias of the $\delta^7\text{Li}$ and $\delta^{11}\text{B}$ measurements using the new AVC protocol were better than 1‰ for samples containing a few tens to a few tens of thousands ppm Li and B. We also report significant local heterogeneity of up to several ‰ found in some basalt glasses, but not in NIST SRM 612 and 610.

 Received 3rd August 2016
 Accepted 26th September 2016

DOI: 10.1039/c6ja00283h

www.rsc.org/jaas

1. Introduction

Lithium and boron each have two naturally occurring stable isotopes: ^6Li (nuclidic mass 6.0151232) and ^7Li (7.0160045), and

^{10}B (10.0129380) and ^{11}B (11.0093053).¹ These isotopes possess large mass differences, resulting in huge isotopic fractionation in natural systems compared with other stable isotopes. In particular, fractionation can alter the stable isotope ratios by as much as several tens permille in low-temperature systems, *e.g.*, chemical precipitation in subaqueous environments or fluid release from solids.^{2,3} The $^6\text{Li}/^7\text{Li}$ and $^{10}\text{B}/^{11}\text{B}$ isotope ratios are usually expressed with δ -notation relative to the National Institute of Standards and Technology (NIST) reference materials SRM 8545 (LSVEC, lithium carbonate) and SRM 951 (boric acid), respectively. The equations for determining the above quantities are:

$$\delta^7\text{Li} = \left[\left(\frac{^7\text{Li}/^6\text{Li}}{^7\text{Li}/^6\text{Li}} \right)_{\text{sample}} / \left(\frac{^7\text{Li}/^6\text{Li}}{^7\text{Li}/^6\text{Li}} \right)_{\text{SRM8545}} - 1 \right] \times 1000 \quad (1)$$

$$\delta^{10}\text{B} = \left[\left(\frac{^{10}\text{B}/^{11}\text{B}}{^{10}\text{B}/^{11}\text{B}} \right)_{\text{sample}} / \left(\frac{^{10}\text{B}/^{11}\text{B}}{^{10}\text{B}/^{11}\text{B}} \right)_{\text{SRM951}} - 1 \right] \times 1000 \quad (\text{ref. } 4) \quad (2)$$

These two stable isotope systems are useful geochemical tracers in solid earth geochemistry, since isotopic fractionation

^aDepartment of Solid Earth Geochemistry, Japan Agency for Marine-Earth Science and Technology (JAMSTEC), 2-15 Natsushima-Cho, Yokosuka, 237-0061, Japan. E-mail: jkimura@jamstec.go.jp; Fax: +81-46-987-9625; Tel: +81-46-967-9765

^bKochi Institute of Core Sample Research, Japan Agency for Marine-Earth Science and Technology (JAMSTEC), 200 Monobe-Otsu, Nankoku City, Kochi 783-8502, Japan

^cCenter for Northeast Asian Studies, Tohoku University, 41 Kawauchi, Aoba-ku, Sendai 980-8576, Japan

† Electronic supplementary information (ESI) available: Fig. S1: heterogeneity of the GSD-1G glass used for B isotope ratio determination; Table S1: analytical results for SRM 612 glass with different ablation parameters; Table S2: analytical results for standard reference materials; Table S3: analytical results for GSD-1G using SRM 612 as a standard; Table S4: analytical results for SRM 612 with reference to ablation crater volume; Table S5: analytical results for jadeite using crater volume-corrected LA-MFC-ICPMS; Table S6: analytical results for tourmaline using crater volume-corrected LA-MFC-ICPMS. See DOI: 10.1039/c6ja00283h

occurs in low-temperature environments ($T = 0\text{--}350\text{ }^{\circ}\text{C}$) such as continental weathering, continent-derived sediment flux in oceans, and low-temperature and hydrothermal alterations of ocean floor basalts and abyssal peridotites.^{2,3} Another type of fractionation occurs during the subduction of oceanic plates containing continental and ocean floor materials. Low to ultra-high grade metamorphic processes release aqueous/supercritical liquids from the subducted materials and fractionate the isotopes in an intermediate temperature range ($T = 350\text{--}850\text{ }^{\circ}\text{C}$).^{5–7} The released slab liquids are manifested in subduction zone aqueous fluids or magmas, which show a partial recovery of these elements.^{8,9} Deep isotope fractionation can only occur beyond subduction zones by subsolidus diffusion at mantle temperatures,¹⁰ since significant fluid release would not occur afterwards; the residual slab materials are mixed with mantle peridotite¹¹ and delivered back to the surface through basalt melts erupted on plume-related oceanic islands.¹² The strong fractionation of Li and B isotopes in metamorphic processes is of particular interest, since it is key for determining the fractionation of elements and isotopes between the Earth's surface and its deep interior.^{2,3}

For metamorphic rock studies, the *in situ* analyses of Li and B isotope ratios are particularly important. The various stages of fractionation are recorded in minerals such as clinopyroxene, with a large substitution of $\text{LiAlSi}_2\text{O}_6$ and tourmaline ($\text{XY}_3\text{Z}_6\text{-(T}_6\text{O}_{18})\text{(BO}_3)_3\text{V}_3\text{W}$, where X = Ca, Na, K, □ (vacancy); Y = Li, Mg, Fe^{2+} , Mn^{2+} , Zn, Al, Cr^{3+} , V^{3+} , Fe^{3+} , Ti^{4+} , □; Z = Mg, Al, Fe^{3+} , Cr^{3+} , V^{3+} ; T = Si, Al, and B; B = B, □; V = OH, O; W = OH, F, O) with B as a major component. Chemical zoning of Li and B isotopes has been used for the interpretation of prograde and retrograde metamorphic processes.^{5–7} Applications using secondary ionisation mass spectrometry (SIMS) are known for B isotopes,^{13,14} but are uncommon for Li isotopes, although both Li and B isotopes were analysed in melt inclusions of olivines from Hawaiian lavas.¹² Laser ablation multiple-collector inductively coupled plasma mass spectrometry (LA-MC-ICPMS) was recently applied to the analysis of both Li and B isotopes in metamorphic minerals.¹⁵

Reports describing $\delta^7\text{Li}$ and $\delta^{10}\text{B}$ analyses by LA-MC-ICPMS are rather rare. Le Roux *et al.* (2004)¹⁶ described a $\delta^{10}\text{B}$ analytical method for glasses and basalt groundmasses using a multiple collector (MC)-ICPMS equipped with two ion counters. Following studies used multiple Faraday collector (MFC)-ICPMS. Tiepolo *et al.* (2006)¹⁷ analysed various geological glass standards with a reproducibility of 4–6‰ two-standard errors (2SE). Miková *et al.* (2014)¹⁸ reported strong isotopic fractionation of B dependent on the sample matrix. Lin *et al.* (2014)¹⁹ examined B isotopic fractionation in radial and axial directions in the ICP with various interface cone setups and additional N_2 gas. Le Roux *et al.* (2010)²⁰ first reported a $\delta^7\text{Li}$ analytical method using a combined Faraday collector ^7Li and ion counter ^6Li system for glass samples. Recently, Martin *et al.* (2015)¹⁵ examined both $\delta^7\text{Li}$ and $\delta^{10}\text{B}$ analytical methods using LA-MFC-ICPMS and reported $\delta^{10}\text{B}$ values for pyroxene, mica, and antigorite metamorphic minerals, whereas $\delta^7\text{Li}$ was determined for pyroxene, mica, and albite. The authors reported strong isotopic fractionation of both B and Li in relation to the signal intensity.

All previous LA-MC-ICPMS studies used a standard bracketing mass bias correction, since the mass dispersion of these isotopes is very large for an ordinal double focusing MC-ICPMS, preventing the application of any external mass bias correction methods valid for transient signals from laser ablation. Le Roux *et al.* (2004 and 2010) used a line raster ablation mode with a $200\text{ }\mu\text{m}$ wide \times $3250\text{ }\mu\text{m}$ long trench and a frequency-quadrupled 266 nm Nd-YAG laser for $\delta^{10}\text{B}^{16}$ and a $150\text{ }\mu\text{m}$ wide \times $500\text{ }\mu\text{m}$ long trench with a 213 nm frequency-quintupled Nd-YAG laser for $\delta^7\text{Li}$.²⁰ No significant isotopic fractionation for $\delta^{11}\text{B}$ was reported between the samples and standard glass materials, but a matrix bias between NIST SRM 61X and basalt glasses was detected for $\delta^7\text{Li}$.^{16,20} In contrast, Miková *et al.* (2014) used a 216 nm Nd-YAG laser with a $50\text{ }\mu\text{m}$ crater diameter and a $200\text{ }\mu\text{m}$ -long trench. Lin *et al.* (2014) and Martin *et al.* (2015) used a 193 nm ArF excimer LA (193ExLA) in a spot mode at crater diameters of 10–175 μm . To date, many studies have reported significant isotopic fractionation for both $\delta^7\text{Li}$ and $\delta^{10}\text{B}$.^{15,18,19} Such fractionation under different laser ablation conditions was not observed for Pb isotopes (^{206}Pb , ^{207}Pb , and ^{208}Pb),^{21,22} but was reported as significant for Cu (^{65}Cu and ^{63}Cu) and Fe (^{54}Fe , ^{55}Fe , and ^{56}Fe) isotopes.^{23–25} However, no fractionation of Cu and Fe isotope ratios between different matrices was reported using infrared or 200 nm femtosecond laser ablation (FsLA).^{26,27} As such, the nature of laser parameter-induced isotopic fractionation is still enigmatic.

Herein, we report the results of a systematic examination of laser parameter-induced mass fractionation for the determination of $\delta^7\text{Li}$ and $\delta^{10}\text{B}$ isotope compositions in synthetic glasses and natural rocks and minerals using 193ExLA and 266 nm FsLA (266FsLA). We varied the laser crater diameter and laser repetition rate, and observed how these parameters affected the isotopic fractionations measured by MFC-ICPMS. The origin of this mass fractionation effect is discussed, and the optimised ablation conditions are examined. After the evaluation of isotopic homogeneity in the NIST SRM 610 and 612 bracketing standards, the application of this method to some basalt glasses is presented. Further, we report analytical results for jadeite and tourmaline minerals with matrices quite different from those of SRM 61X glasses. For this, we propose a novel ablation volume-corrected (AVC) analytical protocol to cope with the laser parameter-induced mass fractionation, applicable to a wide range of sample types.

2. Experimental

2.1. Samples

We used an SRM 612 silica-rich synthetic glass doped with multiple elements (approximately 50 ppm each) as a standard. An SRM 610 glass (approximately 500 ppm of each element) was used as an unknown or standard. BHVO-2 G, BCR-2G, and GSD-1G basalt glasses, issued by the United State Geological Survey (USGS), and solid rock slabs of JB-2 and JB-3 from the Geological Survey of Japan (GSJ) were used as unknowns. The reported Li and B concentrations and $\delta^7\text{Li}$ and $\delta^{10}\text{B}$ isotope compositions have previously been published.⁴ All samples were surface-polished, cleaned with ethanol, and immediately subjected to

LA-MFC-ICPMS analysis. Jadeite and tourmaline mineral samples originated from the New Idria serpentinite body, California^{28,29} and Ishikawa-yama granitic pegmatites, Japan,³⁰ respectively. These were sawed in half and mounted on a slide glass with epoxy resin. The opposite side was sawed to form a thick slab section, and the surface was polished with diamond paste for better observation.

2.2. Instrumental setup

The instrumentation and setup for 266FsLA, 193ExLA, and MFC-ICPMS are described in the following sections.

2.2.1. 266 nm FsLA. The 200/266 nm FsLA system (OK-Fs2000K, OK Laboratory, Tokyo, Japan) was provided by the Japan Agency for Marine-Earth Science and Technology (JAMSTEC). The UV-FsLA system was equipped with a Solstice one-box Ti-sapphire femtosecond regenerative amplifier (Spectra-Physics, Santa Clara, CA, USA) using TP-1A THG and TP-1A FHG frequency tripling and quadrupling harmonic generators (Spectra-Physics, Santa Clara, CA, USA). Details of this system have been reported elsewhere.³¹ A wavelength of 266 nm alone was used to achieve the necessary sampling volume. The laser beam diameter was altered to 30, 40, 70, and 90 μm . The laser fluence on the sample surface was $\sim 12 \text{ J cm}^{-2}$. A rotating raster ablation protocol³¹ was used for different beam sizes along the circumference of a circle with radii of 20, 30, 50, and 70 μm at a velocity of $\sim 10 \mu\text{m s}^{-1}$. This method produced craters with diameters of 30, 50, 100, and 200 μm , respectively. The laser repetition rate was varied at 10, 20, 30, 50, and 100 Hz, generating crater depths of ~ 8 , ~ 15 , ~ 38 , ~ 75 , and $\sim 150 \mu\text{m}$, respectively, after 35 s of ablation. The use of the rotating raster protocol for 266FsLA produced a quasi-cylindrical crater with an undulated bottom surface due to the Gaussian energy profile of the laser. All operation parameters are listed in Table 1.

2.2.2. 193 nm ExLA. The 193ExLA system used a Com-Pex102 laser source (Coherent, Gottingen, Germany) with imaging laser delivery optics (OK-ExLA2000, OK Laboratory, Tokyo, Japan).³² The system was operated with a fluence of ~ 20 and $\sim 12 \text{ J cm}^{-2}$, with crater diameters of 30, 50, 100, and 200 μm at repetition rates of 1, 2, 5, 10, and 20 Hz. The resultant crater depths were ~ 8 , ~ 15 , ~ 40 , ~ 75 , and $\sim 150 \mu\text{m}$ after 35 s for all crater diameters (Table 1). The craters generated by 193ExLA were all cylindrical with a flat-bottomed surface. The depositions around the laser craters obtained with 193ExLA were thick and widespread. In contrast, thin and almost invisible depositions were generated using the 266FsLA.³¹ Helium (1.15 L min^{-1} flow rate) was used as the laser aerosol carrier gas throughout the experiments (Table 1).³³

2.2.3. MFC-ICPMS. The 266FsLA or 193ExLA units were coupled with a modified Neptune MFC-ICPMS (Thermo Fisher Scientific, Bremen, Germany) at JAMSTEC. Helium ablation gas was mixed with Ar sample gas (1.2 L min^{-1}) in a cylindrical mixing chamber (70 cm^3 inner volume) immediately before reaching the ICP torch.³¹ The MFC-ICPMS interface was modified by the addition of a high-efficiency rotary pump for high ion transmission.³² The JET-sampler and X-skimmer cones were

used along with the guard electrode (GE), resulting in the best sensitivity ever achieved (Table 1).^{19,34}

We assigned ${}^6\text{Li}^+$ and ${}^7\text{Li}^+$ to L4 and H4 Faraday collectors, respectively, using zoom ion optics (ZOP) at a dispersion quad lens voltage of $\sim 17.8 \text{ V}$ and a focus quad lens voltage of $\sim 0 \text{ V}$. A dispersion quad ZOP was required, since our Neptune instrument was equipped with multiple ion counter arrays outside L4 and H4. The axial Faraday mass was set to $M \approx 6.5$, which was used as a dummy mass. The ${}^{10}\text{B}^+$ and ${}^{11}\text{B}^+$ were set to L4 and H4 Faraday collectors without using the dispersion quad ZOP, and the axial Faraday mass was set to $M \approx 10.5$. This setup produced flat-top peaks for all isotopes in the low mass resolution mode ($M/\Delta M \approx 400$). The ${}^{12}\text{C}^{2+}$ peak was detected close to the ${}^6\text{Li}^+$ peak, but they did not overlap at the nominal mass number, whereas the ${}^{14}\text{N}^{2+}$ peak partially overlapped with the ${}^7\text{Li}^+$ peak, resulting in a higher baseline at $\sim 0.002 \text{ V}$. Due to this interference, additional N_2 gas¹⁹ was not considered even for B. The peak attributed to the Ar gas impurity, ${}^{20}\text{Ne}^{2+}$, appeared close to the ${}^{11}\text{B}^+$ peak, but no significant overlap was observed with ${}^{10}\text{B}^+$ and ${}^{11}\text{B}^+$, resulting in fairly low gas blanks of $\sim 0.001 \text{ V}$, same as for ${}^6\text{Li}^+$. These results allowed the low mass resolution mode to be used for high ion transmission in MFC-ICPMS.

All Faraday collectors were connected to ordinal Faraday amplifiers using a $10^{-11} \Omega$ resistor. The use of high-gain $10^{-12} \Omega$ amplifiers did not improve the in-run analytical precision in the signal intensity range of 0.01–5 V used in this study. Additionally, $10^{-13} \Omega$ amplifiers did not accommodate the signal range due to their limited quantification range ($< \sim 0.01 \text{ V}$).²² High-gain Faraday amplifiers were better suited to smaller sample sizes, but the achievable precision (a few permille dependent on signal intensities) limited their application.²²

2.3. Data acquisition and correction

We employed simple on-peak gas blank reduction and time-resolved data acquisition (TRA) in this study.^{15,16,20} Data correction was performed off-line using an Excel spreadsheet.

2.3.1. Data acquisition. Fig. 1 shows an example of data acquisition and correction protocols for B isotope ratio measurements, with the same protocol used for Li isotope ratio measurements. The TRA comprised 200 scans of $\sim 0.524 \text{ s}$ for data acquisition. Acquisition began without laser ablation, and the instrumental baselines including gas blanks (GB1) were recorded based on the last seven of the first 30 scans. Next, the laser was fired, with the first 17 scans used for signal stabilisation followed by 43 sample signal acquisition scans. The laser was turned off, and the last 15 of the 200 total scans were used for the second gas blank (GB2) after the complete washout of sample signals in 94 scans (Fig. 1a and b and Table 1). Net ${}^{10}\text{B}^+$ and ${}^{11}\text{B}^+$ intensities were subsequently calculated using the averaged GB1 and GB2 intensities with linear interpolation of the gas blank values for each of the 43 signal scans. The use of GB1 and GB2 taken immediately before signal acquisition and immediately after the washout, respectively, ensured the correction of drifts in the gas blanks caused by the instrumental drift and decreasing cone memory with time after laser ablation. This was especially required in the case of Li. Using the

Table 1 Laser and mass spectrometer setup parameters for the 266FsLA/193ExLA-MFC-ICPMS^a

Apparatus	Experimental setting
[Femtosecond laser ablation system]	
Equipment	OK-Fs2000K OK Laboratory Ltd.
Source wave length/pulse width	266 nm/~170 fs
Energy at source	350 μJ
Focusing lens	Fused-silica aspherical objective lens
Spot size	30, 40, 70, 90 μm
Fluence at laser spot	~12 J cm ⁻²
Repetition rate	10, 20, 30, 40, 50, 100 Hz
Rotation raster radius	20, 30, 50, 70 μm
Rotation raster velocity	10 μm s ⁻¹
Final crater size	30, 50, 100, 200 μm
He gas flow	1.15 L min ⁻¹
[Excimer laser ablation system]	
Equipment	OK EX2000 OK Laboratory Ltd.
Source wave length/pulse width	193 nm/~20 ns
Energy at source	~200 mJ
Focusing lens	Fused-silica imaging optics using field lens and air spaced doublet objective lenses
Spot size	30, 50, 100, 200 μm diameter
Fluence at laser spot	~20 and ~12 J cm ⁻²
Repetition rate	1, 2, 5, 10, 20 Hz
He gas flow	1.15 L min ⁻¹
[MC-ICPMS]	
Equipment	Thermo Scientific Neptune
RF-power	1200 W
Guard electrode	On
Sampling cone	JET-sample cone (Ni)
Skimmer cone	X-skimmer cone (Ni)
Plasma gas (Ar)	1.0 L min ⁻¹
Laser carrier gas (He)	~1.15 L min ⁻¹
Interface vacuum with E2M80	1.7 mbar with He ablation carrier gas
Baseline measurement	On peak baselines
Acquisition	~0.524 s × 200 scans for time-resolving analysis including 30 scans for first gas blank (GB1) 17 scans for signal stabilization 43 scans for isotope data acquisition 94 scans for washout 15 scans for second gas blank (GB2)
Faraday collector setting	
<i>[Li isotopes]</i>	
⁶ Li ⁺	FC L4 (10 ¹¹ Ω amplifier)
^{6.5} M dummy mass	FC centre (10 ¹¹ Ω amplifier)
⁷ Li ⁺	FC H4 (10 ¹¹ Ω amplifier)
Zoom optics 1: dispersion quad lens	17.8 V
Zoom optics 2: focus quad lens	-1 V
<i>[B isotopes]</i>	
¹⁰ B ⁺	FC L4 (10 ¹¹ Ω amplifier)
^{10.5} M dummy mass	FC centre (10 ¹¹ Ω amplifier)
¹¹ B ⁺	FC H4 (10 ¹¹ Ω amplifier)

Table 1 (Contd.)

Apparatus	Experimental setting
Zoom optics 1: dispersion quad lens	0 V
Zoom optics 2: focus quad lens	+6 V
Data correction	Off-line with Excel spreadsheet

^a FC: Faraday collector.

43 sets of net ¹⁰B⁺ and ¹¹B⁺ intensities, average ¹¹B/¹⁰B isotope ratios and 2SE values were calculated. The same calculations were applied to Li isotopes. It should be noted that no detectable downhole isotopic fractionation was observed throughout the study. This was true for both the 266FsLA and 193ExLA systems (see Fig. 1c).

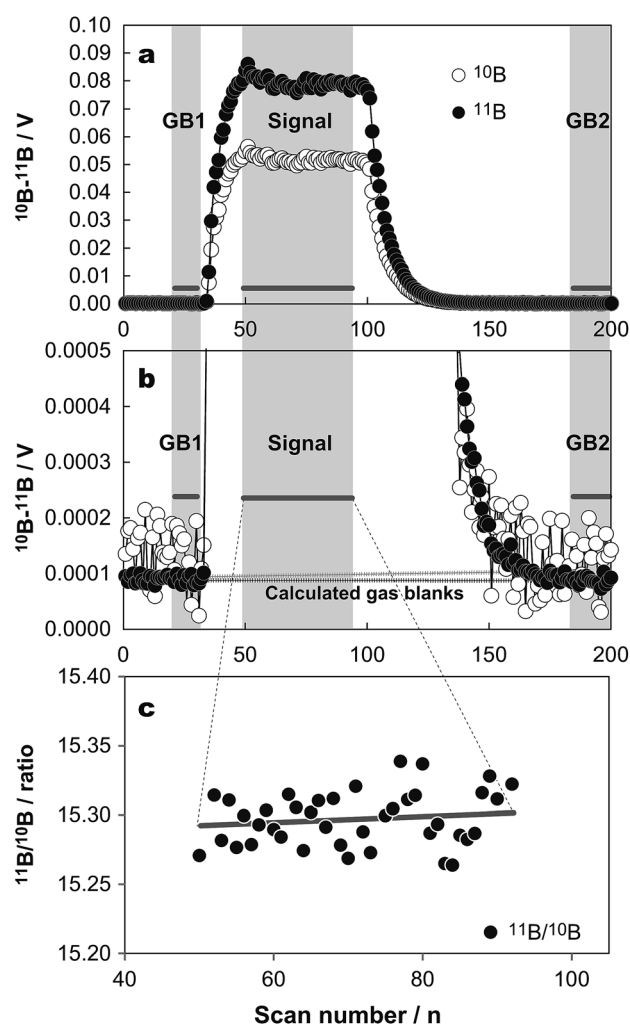


Fig. 1 Signal profiles of B isotopes acquired from a single crater. GB1 and GB2 indicate time-resolved data used for gas blanks. Gas blanks were calculated by linear interpolations between the two blanks (a). The acquired signals were corrected for the gas blanks, and B isotope ratios were calculated (b and c). The signal profile was taken from the SRM 612 standard glass using a 100 μm diameter crater at a 5 Hz laser repetition rate with 193ExLA. Note that no downhole isotope ratio fractionation was observed.

2.3.2. Data correction. An ordinal standard-sample bracketing method^{21,22} was used. The 43 gas blank-corrected isotope ratios from an unknown sample spot were first corrected for the mass bias factor (α), determined from the average of two measurements of SRM 612 or SRM 610 conducted immediately before and after the unknown, using the equations below (eqn (3) and (4) for Li; eqn (5) and (6) for B):

$$\alpha = \frac{({}^7\text{Li}/{}^6\text{Li})_{\text{std.ref.}}}{\text{avg}({}^7\text{Li}/{}^6\text{Li})_{\text{std.meas.}}} \quad (3)$$

$$({}^7\text{Li}/{}^6\text{Li})_{\text{corrected}} = ({}^7\text{Li}/{}^6\text{Li})_{\text{sp.meas.}} \times \alpha \quad (4)$$

$$\alpha = \frac{({}^{11}\text{B}/{}^{10}\text{B})_{\text{std.ref.}}}{\text{avg}({}^{11}\text{B}/{}^{10}\text{B})_{\text{std.meas.}}} \quad (5)$$

$$({}^{11}\text{B}/{}^{10}\text{B})_{\text{corrected}} = ({}^{11}\text{B}/{}^{10}\text{B})_{\text{sp.meas.}} \times \alpha \quad (6)$$

where std_ref. is the reference isotope ratio of the standard, std_meas. refers to the measured isotope ratios in the standard, corrected refers to the mass fractionation-corrected isotope ratios of the unknown, and sp_meas. refers to the measured isotope ratio of the unknown.

The Li isotope standard reference values were ${}^7\text{Li}/{}^6\text{Li} = 12.553$ for SRM 612 and ${}^7\text{Li}/{}^6\text{Li} = 12.568$ for SRM 610,³⁵ while those for B were ${}^{11}\text{B}/{}^{10}\text{B} = 4.042$ for SRM 612 (ref. 36) and ${}^{11}\text{B}/{}^{10}\text{B} = 4.048$ for SRM 610.³⁷ The mass bias-corrected 43 isotope ratios were normalised using δ -notation, having reference isotope compositions of ${}^7\text{Li}/{}^6\text{Li} = 12.173$ for SRM 8545 (lithium carbonate, L-SVEC)³⁸ and ${}^{11}\text{B}/{}^{10}\text{B} = 4.048$ for SRM 951 (boric acid).³⁹ These reference values were used to obtain $\delta^{11}\text{Li}$ and $\delta^{11}\text{B}$ values using eqn (1) and (2), and the 43-scan average measured values and 2SEs were calculated. The δ -notation SRM glass standard values were $\delta^{11}\text{Li} = 31.2$ (ref. 35) and $\delta^{11}\text{B} = -0.51$ for SRM 612,⁸ and $\delta^{11}\text{Li} = 32.5$ (ref. 35) and $\delta^{11}\text{B} = -0.74$ for SRM 610.³⁷

3. Results and discussion

In this section, we first examine the analytical results for SRM 612 to evaluate LA parameter-dependent mass fractionation, and then turn to the basalt glass/groundmass standard reference materials to evaluate the performance of the optimal ablation setup.

3.1. Li and B isotopic fractionation: previous studies

Miková *et al.* (2014, for B) and Martin *et al.* (2015, for Li and B) reported systematic and significant mass bias originating from different ablation parameters using 193ExLA.^{15,18} Earlier, Le Roux (2010) reported the importance of matrix matching for Li isotope ratio determination using 213 nm YAG LA.²⁰ Martin *et al.* (2015) reported negative correlations between signal intensities and $\delta^{11}\text{Li}$ or $\delta^{11}\text{B}$ values. These isotopic fractionations had values of as much as $\pm 4\%$, corresponding to a *ca.* eight-fold change in signal intensities for both Li and B isotopes.¹⁵ According to Martin *et al.* (2016), these isotopic

fractionations were linearly correlated with signal intensity for both $\delta^{11}\text{Li}$ and $\delta^{11}\text{B}$ when the laser fluence and repetition rate were kept constant at $\sim 10 \text{ mJ cm}^{-2}$ and 10 Hz, respectively, with an altered laser crater diameter of 25–75 μm for Li isotopes and 65–125 μm for B isotopes. The authors also reported that the correlation slope showed an inter-day variability for Li isotopes and that the linear correlations were violated with smaller crater diameters ($< 25 \mu\text{m}$) for both isotopes. Lin *et al.* (2014) tested various interface cones and N_2 gas flow rates for B isotopes. ICP isotopic fractionation was examined in axial and radial directions with and without the addition of N_2 .¹⁹ A significant reduction of isotopic fractionation by additional N_2 was demonstrated, but the laser-parameter bias was not discussed fully.

Overall, the previous studies reported laser parameter-induced bias at a high ICP sample loading, attributed to obtaining enough analytical repeatability for samples with a low Li/B content. Insufficient precision at a ± 2 –6‰ level prevented detailed examination. This is frustrating, since the higher analysis precision (sample loading) allows greater isotopic fractionation to occur. We examine the details of laser parameter-induced bias in the following section.

3.2. Nature of the observed laser ablation fractionation

Fig. 2a–d illustrate the correlations between averaged signal intensities and isotope ratios ($\delta^{11}\text{Li}$ or $\delta^{11}\text{B}$) for 193ExLA and 266FsLA (raw data are in ESI Table S1†). As noted by Martin *et al.* (2015), quasi-linear negative correlations between the laser repetition rate and isotope ratios were observed for a given laser crater diameter. This correlation was lost for 30 μm craters, in agreement with the previous report.¹⁵ Furthermore, we found that a systematic difference in crater diameter was best represented with Li isotopes using 193 ExLA (Fig. 2a). B isotopes showed the same fractionation, but to a lesser extent for craters of 30–100 μm , and with the exception of the 200 μm crater (Fig. 2b). The responses of 266FsLA were different, showing an almost linear correlation for Li isotopes at all crater sizes, apart from the low signal region (Fig. 2c). Negative correlations were common, but the slopes were systematically different for the 50, 100, and 200 μm craters (Fig. 2c and d). In general, negative slopes were common irrespective of the laser type, ablation protocol, and crater diameter. However, the responses were non-linear for all laser ablation parameters.

Fig. 2e–h show the plots of the laser beam aspect ratio *vs.* isotope fractionation. The aspect ratio is defined as the crater depth divided by its diameter ($d/2r$). The laser beam size was used in preference to the crater size, since 266FsLA possessed an almost half-diameter laser beam with a rotating raster (Table 1). Excellent linear correlations were common between $d/2r$ and $\delta^{11}\text{Li}$ or $\delta^{11}\text{B}$ in craters of $> 50 \mu\text{m}$. Small craters (10–30 μm) did not show any systematic correlation (Fig. 2e–h). The slopes were flatter for smaller craters, becoming increasingly steeper for larger ones. For 193ExLA, the slopes were always steeper for Li (Fig. 2e and g) than for B (Fig. 2f and h).

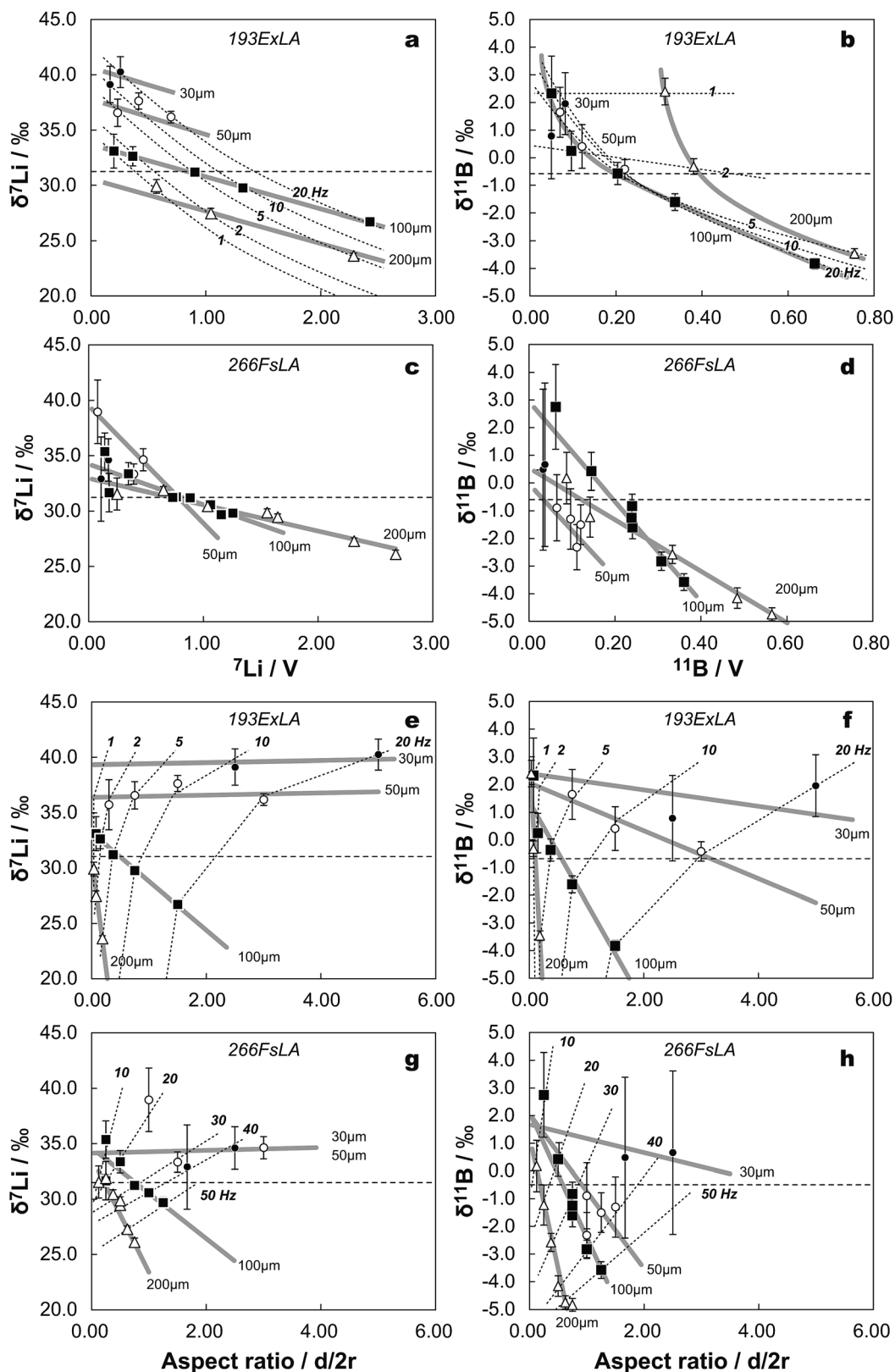


Fig. 2 Isotope fractionation of B and Li induced by different crater sizes (shaded lines) and repetition rates (dotted lines). The results show that isotopic fractionation is non-linear and controlled by mass fractionation at the LA site and inside the mass spectrometer in the ICP (a–d). Linear correlations with aspect ratios suggest ablation fractionation, whereas different slopes for various crater sizes suggest an ICP mass loading effect (e–h). Note, that normal LA can maintain a sampling efficiency within a 1.5-fold difference between the mineral/basalt sample and the NIST 612 standard, indicating that ablation-induced mass fractionation is limited to <1‰ in practice. The aspect ratio is defined as the ratio of the diameter (d) to the radius (r) of the laser crater. Notably, both 193ExLA and 266FsLA showed similar results.

3.3. Origin of mass fractionation

Strong isotopic fractionation is obviously caused by some laser parameters, with identification of its source being essential for high-precision analyses of Li and B isotopes. A number of sources for isotopic fractionation are available in LA-MFC-ICPMS. First, isotopic fractionation can occur at the LA site due to the generation of molten samples by the laser heat (thermal fractionation).^{33,40} The released vapour phase and finer aerosols condensed from the LA site exhibit lighter isotope ratios due to the selective vaporisation of lighter isotopes.²⁴ Second, isotopic fractionation occurs in the ICP when large ablation particles are insufficiently vaporised⁴¹ due to the lowering of the plasma temperature by mass loading of the laser aerosols,²⁴ leading to selective vaporisation of lighter isotopes.⁴² Moreover, the space charge effect can fractionate isotope ions at the skimmer cone or in the ion optics.^{42,43} Among these possibilities, ICP mass loading and thermal fractionation at the LA site are the primary and secondary sources, the effects of which are discussed below.

3.3.1. Mass loading – low plasma temperature – Rayleigh fractionation. The major factor in laser parameter-induced fractionation is the increasing lighter isotope fraction with increasing ICP sample loading. Sample loading has an almost linear effect on isotope fractionation when the laser repetition rate is changed at a given crater diameter (Fig. 2a–d). The overall range of mass fractionation was limited to $\pm\sim 5\%$ for $\delta^7\text{Li}$ and $\pm\sim 4\%$ for $\delta^{11}\text{B}$ in response to an ~ 12 -fold signal intensity change (*i.e.*, mass loading) (Fig. 2a–d). This is in agreement with a previous study using the same MFC-ICPMS instrument with a different sampling interface, *i.e.*, using H–N cones rather than the JET–X cones utilised in this study.¹⁵ The particle size distributions of laser aerosols from 193ExLA and 266FsLA were identical in terms of the most populated particle sizes.³¹ Therefore, isotopic fractionation occurred mainly in the ICP for different LA systems. Lighter mass fractionation has also been reported in solution-phase MFC-ICPMS. Andren *et al.* (2004) measured the $^{11}\text{B}/^{10}\text{B}$ ratio for a ~ 10 ppm B solution in a splay chamber drain, on the surface deposits of the sampler and skimmer cones. These deposits showed a significantly greater light mass fractionation, up to $\sim 10\%$, than the ones on the sampler and skimmer cone front surfaces.⁴² Jackson and Günther (2003) confirmed the absolute lighter isotope fractionation of Cu in the ICP.²⁴ Lighter mass fractionation in the ICP is thus common, irrespective of the solution/LA sample introduction mode and variable ion interface setup.

Radial ICP isotope fractionation was observed earlier in solution mode for $^{65}\text{Cu}/^{63}\text{Cu}$ (Jackson and Günther, 2003)²⁴ and recently in LA mode for $^{11}\text{B}/^{10}\text{B}$ (Lin *et al.*, 2014).¹⁹ Both reports showed lighter mass fractionation towards the perimeters, forming a convex-up pattern across the ICP (Fig. 3). This occurred at a limited distance of ± 0.7 mm from the torch axis in the solution mode. Heavier isotope fractionation of up to $+6\%$ occurred in the ± 0.7 – 1.2 mm outer zones (thick grey lines in Fig. 3).²⁴ The results of our measurements for Li and B isotopes were similar to those of Lin *et al.* (2014). The profile was always convex-up until ± 1.75 mm distance from the torch axis (Fig. 3b and d), due to use of He carrier gas in both LA modes in contrast

to Ar in the solution mode by Jackson and Günther (2003). He carrier gas expanded the low-temperature plasma conduit (dark region), forming the wider convex-up zone (Fig. 3b and d).

Li and B isotope measurements shared three common features, the first being the above convex up patterns. The second feature was the strongly suppressed axial isotope ratios at a high mass loading from 200 μm craters. The third feature was the narrower convex-up patterns at a low mass loading from 100 μm craters (Fig. 3b and d). The zone with a maximum analyte density was located at the torch axis, with higher dispersal rates for lighter isotopes.^{44,45} This radial dispersion model explains the overall convex-up profiles (feature 1). If the isotope ratio suppression were caused by a lower plasma temperature, then the lower $\delta^7\text{Li}$ in the axial region would correlate with high mass loading (features 2 and 3, Fig. 3b). This was less clear for $\delta^{11}\text{B}$, where high mass loading exhibited a less suppressed outermost zone, while the response in the axial region was identical to that of $\delta^7\text{Li}$ (Fig. 3d). This suggests effective vaporisation of B in the high-temperature plasma sheath (outer zone) during mass loading, due to the outward expansion of the high-density analyte centre.

Lighter mass fractionation due to low temperature is explained by Rayleigh fractionation. The loading of the plasma with larger LA particles led to insufficient (partial) fusion,⁴¹ resulting in selective vaporisation of the lighter isotopes. Mass loading also lowers the plasma temperature due to the consumption of latent heat, since a large amount of aerosol is melted in the ICP.^{41,46} Jackson and Günther (2003) reported $^{65}\text{Cu}/^{63}\text{Cu}$ isotope fractionation and found that the filtered fine aerosol particles (< 0.5 μm) were lighter owing to ablation fractionation. However, the authors also reported that a much greater lighter mass fractionation occurred in the ICP, even for filtered fine aerosols.²⁴ This observation was rationalised by the insufficient vaporisation in the low-temperature ICP.

The reduction of ICP temperature was estimated by a study on the origin of the matrix effect for elemental fractionation. Kimura *et al.* (2012) calculated apparent ionisation temperatures from the elemental ionisation efficiencies of silica-rich SRM 612 and Fe-rich basalt glasses.³¹ The authors showed that apparent ionisation temperatures as low as ~ 2000 K were found for easily ionised elements. This was attributed to the different thermal conductivity of glass aerosols with different matrices. The study indicated that mass loading readily lowered the plasma temperature by > 2000 K even for LA craters of 50 μm diameter.³¹ This phenomenon significantly enhances the lighter mass fractionation of Li and B in the ICP for 100–200 μm crater diameters (see Fig. 3).

3.3.2. Thermal effect – molten sample – Rayleigh fractionation. Thermal fractionation at the laser crater is a secondary factor influencing laser-parameter induced fractionation. The aspect ratios of craters increased with their decreasing diameter at a given LA repetition rate (Fig. 2e–h abscissa and thin solid lines). The extent of isotopic fractionation increased with both increasing crater diameter and repetition rate representing increased mass loading to the ICP (Fig. 2e–h vertical axes and thick grey lines with various slopes). These observations implied that the aspect ratio was not the

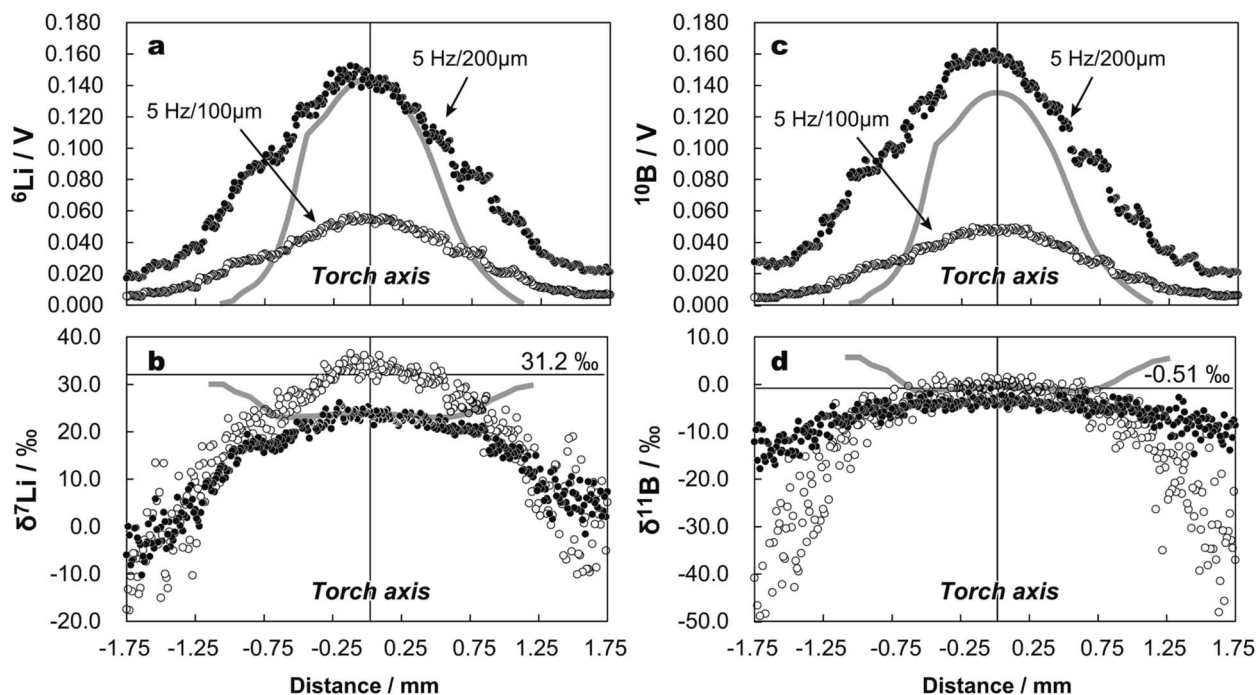


Fig. 3 Radial signal intensities of Li (a) and B (b) and fractionation of Li (c) and B (d) isotopes across the ICP torch. The torch axis corresponds to the highest analyte density. Signal intensities decrease outwards with increasing lighter isotope fractionation. Stronger fractionation occurs at higher sample loading, as shown by lower isotope ratios in the 200 μm crater. The degree of radial fractionation is smaller at high mass loadings, indicating flatter isotope profiles in 200 μm cases. Note that mass bias corrections were made by standard bracketing using spot analyses for 100 μm craters. As a result, the axial isotope ratios were identical to the glass reference values. The operating conditions were 5 Hz, 100 and 200 μm crater diameter, and 193ExLA. Single dots result from 0.512 s scans. Shaded lines represent data of Andren *et al.* (2004) for Cu isotopes for comparison.⁴²

main factor for isotopic fractionation. However, the observed features provided additional insights.

Isotopic fractionation can result from molten surfaces on the laser crater walls. This is prominent for 193ExLA, where a quenched glass layer with thermal cracks develops on the vertical crater walls,^{33,40} whereas it is not observed for 266FsLA.⁴⁰ Molten glass releases lighter isotopes into the vapour phase due to Rayleigh fractionation. Both B and Li behave as volatiles at the melting temperature, enhancing the effect.⁴⁷ Accordingly, the thermal fractionation should be more pronounced for 193ExLA. The larger variation due to different crater diameters in 193ExLA clearly demonstrate this effect (thick shaded lines in Fig. 2a–d).

The bimodal particle size distribution (0.01–0.5 μm and >0.5 μm) in 193ExLA^{48–51} is an important factor for isotopic fractionation caused by the thermal effect at the LA site. We analysed coarse laser particles deposited around the 193ExLA crater^{31,40} dug on SRM 612 by a linear surface raster. The results showed a *ca.* +1.5‰ $\delta^{11}\text{Li}$ fractionation in the deposits (Fig. 4a), resulting in a lighter-mass enrichment of the finer aerosol or the gaseous phases that preferentially reached the ICP. The same lighter mass fractionation was also demonstrated by filtering experiments of the ablated aerosols for Cu isotopes.²⁴ This effect was insignificant for $\delta^{11}\text{B}$ (Fig. 4b), consistent with the smaller aspect ratio differences between 193ExLA and 266FsLA (Fig. 2f and h).

Compared with the large fractionation of *ca.* –8‰ in the ICP, the effect of thermal fractionation was subordinate (Fig. 4). In

fact, the volume of the near-crater deposits is several orders of magnitude smaller than that of the total ablation volume. The crater aspect ratio is related to the origin of downhole elemental fractionation.⁵² However, the downhole fractionation of isotope ratios was insignificant for both Li and B (Fig. 1). We thus think that particle size fractionation is the main process of the thermal fractionation at the LA site.

3.3.3. Other sources of fractionation. Other isotope fractionation mechanisms cannot cause the observed mass fractionation. Insufficient ionisation occurs due to an increase in electron number density or the lowering of ICP temperature.^{31,53} However, these effects on isotope ratios are trivial, since the isotopes in ${}^6\text{Li}/{}^7\text{Li}$ and ${}^{10}\text{B}/{}^{11}\text{B}$ pairs have identical ionisation energies. The spectroscopically measured ionisation potential of Li is $43\,487.167 \pm 0.004 \text{ cm}^{-1}$ (equivalent to $\sim 5.4 \text{ eV}$),⁵⁴ and that of B is $66\,928.10 \pm 0.1 \text{ cm}^{-1}$ ($\sim 8.3 \text{ eV}$),⁵⁵ these values theoretically being almost identical for the corresponding isotopes.^{54,55}

The space charge effect has an opposite influence, increasing the heavier mass transmission in the ion beam axis at the skimmer cone or in the ion optics due to the repulsion forces between positively charged ions.⁵⁶ This was observed for B, where deposition of heavier isotopes was found on the back surface of the skimmer cone and on the extraction lens behind it,⁴² possibly counterbalancing the lighter isotope fractionation in the ICP and at the LA site. This phenomenon complicates the response of LA-MFC-ICPMS. The use of a guard electrode (GE-connected) enhanced mass fractionation.⁴²

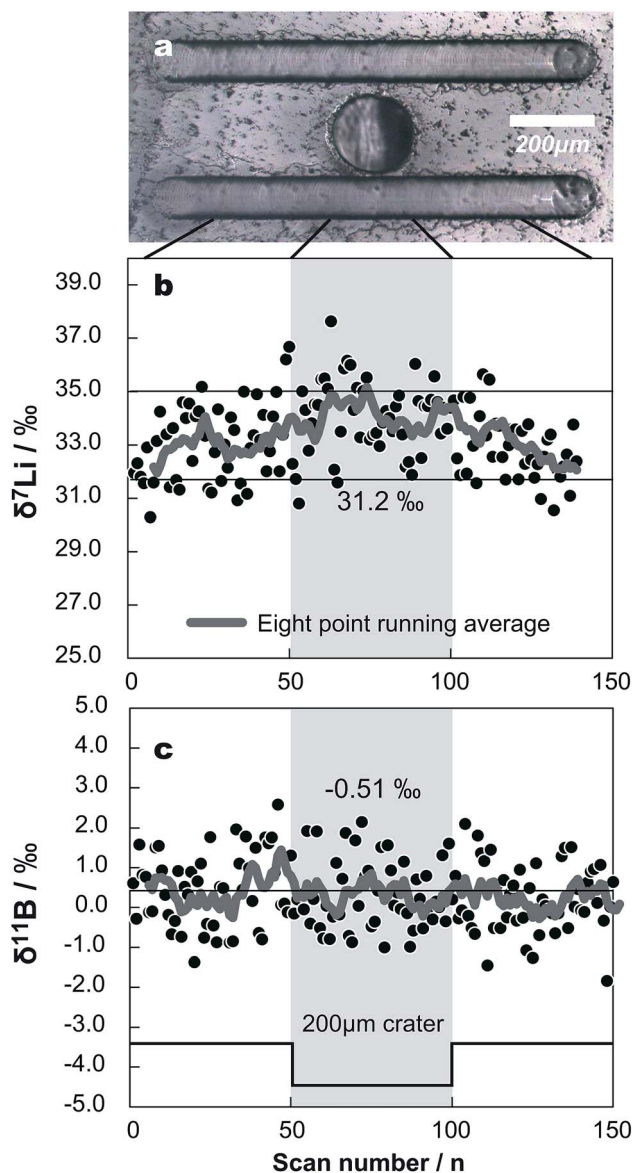


Fig. 4 Line scan profiles of Li and B isotope compositions measured across the laser deposit formed from a 200 μm crater on the SRM 612 glass (a). Heavier isotope ratios are obtained in the thick deposit region for Li isotopes (b), but not for B isotopes (c).

An additional source of fractionation is the matrix effect. Le Roux (2010) analysed basalt glasses using the SRM 612 glass as a standard and found a systematic bias for Li isotopes (Table 2).²⁰ Miková *et al.* (2014) also reported significant isotopic fractionation of B between SRM 610 and tourmaline.¹⁸ Different matrices lead to different LA sampling efficiencies and thus different mass loadings. Different thermal conductivities by different matrices can also lead to different vaporisation properties at the LA site and in the ICP. These phenomena are further discussed in Sections 4 and 5.

3.3.4. Overall effect. The ICP mass loading and ablation fractionation at the LA site both cause lighter mass fractionation. However, these effects appear to be non-linear, as supported by the lack of a linear correlation at low mass loadings,

the non-linear correlations with fractionation factors, and the different slope factors for different crater sizes and laser types (Fig. 2). Combined with some counter-effects, the overall mass fractionation in LA-MFC-ICPMS is certainly unpredictable and difficult to formulate. It is noteworthy, however, that this is the case for lighter elements ($M < 84$) with larger isotopic mass dispersions.^{21,22,24} Optimisation of ablation conditions or analytical protocols is thus required for accurate Li and B isotope analyses. Thus, we attempted to optimise the ablation conditions (Section 4) and develop a novel ablation volume correction (AVC) analytical protocol (Section 5).

4. Isotope compositions of standard basalt glasses

Given the complexities noted above, a practical way to minimise isotopic fractionation is to maintain the ablation conditions, *i.e.*, sampling rate and aspect ratio, between the bracketing standard and bracketed unknown constant. It is clear that a simple adjustment of signal intensity¹⁵ cannot compensate isotopic fractionation. The best option is to use a matrix-matched standard, as recommended in a previous Li isotope study.²⁰ In fact, the characterisation of SRM 610 using SRM 612 as a standard showed the best performance in terms of repeatability and laboratory bias (Table 2). It is questionable, however, how optimised ablation conditions are effective for different matrices, such as silica-rich SRM 61X and basalt glasses.

4.1. Optimisation of ablation conditions

We analysed various standard basalt glasses (BCR-2G, BHVO-2G, and GSD-1G) and basalt groundmasses (JB-2 and JB-3) using SRM 612 as the standard and found that the use of 266FsLA resulted in greater bias due to the poor reproducibility of the laser crater shape. This was caused by the deeper penetration in the beam centre due to the Gaussian energy profile (not shown). Although the rotating raster protocol improved the reproducibility of the crater shape, the undulating bottom surfaces made controlled ablation difficult. Hereafter, we only examine 193ExLA.

Due to the low element abundance in basalt glasses (several to several tens ppm), we used a laser beam with a 100 μm diameter and a *ca.* 20 J cm^{-2} fluence at a repetition rate of 5 Hz, which resulted in 40 μm -deep craters after 35 s. This spatial resolution is superior to those of previous studies (*e.g.*, 250–175 μm craters for Faraday collectors for B and Li isotopes)^{15,16,20} and was accomplished by the enhanced sensitivity ($\sim 2500 \text{ V ppm}^{-1}$ in solution mode for ^7Li using an Aridus II desolvating nebuliser) obtained using a large rotary pump at the interface and JET sampler-X skimmer cones with a GE.^{22,34} The effect of isotopic fractionation was similar to that for the normal settings of the same instrument.¹⁵ The negative effect of high-efficiency ion interfaces was negligible, unlike that of mass-independent isotope fractionation due to oxide formation,^{57,58} which was significant in the case of Nd isotopes.³²

Table 2 Li and B isotope compositions for standard reference materials^a

Sample	$\delta^7\text{Li}$ relative to SRM 8545	$\delta^{11}\text{B}$ relative to SRM 951
SRM 612	+31.2 (ext. standard)	−0.51 (ext. standard)
Reference	+31.2 ± 0.1 (Kaseman <i>et al.</i> 2005) ³⁵	−0.51 ± 0.52 (GeoReM mean) ⁶⁵
BCR-2G	+4.07 ± 4.70 (2SD, <i>n</i> = 18)	−3.83 ± 2.58 (2SD, <i>n</i> = 10)
Reference	+3.48 ± 1.71	N/A
BHVO-2G	+7.54 ± 4.64 (2SD, <i>n</i> = 5)	n.a.
Reference	+5.90 ± 5.66	N/A
JB-3	+3.96 ± 9.20 (2SD, <i>n</i> = 5)	n.a.
Reference	+3.94 ± 1.00	N/A
JB-2	n.a.	+7.90 ± 2.06 (2SD, <i>n</i> = 25)
Reference	+4.54 ± 0.69	+7.24 ± 0.33
GSD-1G	+29.2 ± 5.6 (2SD, <i>n</i> = 20)	+10.5 ± 1.9 (2SD, <i>n</i> = 11)
Reference	+31.0 ± 2.3	+10.3 ± 1.3
SRM 610	+31.4 ± 1.0 (2SD, <i>n</i> = 3)	−0.33 ± 0.28 (2SD, <i>n</i> = 5)
Reference	+32.5 ± 1.5	−0.52 ± 0.53

^a Results and errors are given in ‰. Errors in this work are given in 2SD. Reference values are from Brand *et al.* (2014).⁴ Ext. standard: external standard, N/A: not available, n.a.: not analysed. SRM 8545 value of 12.17 from Kasemann *et al.* (2005).³⁵ SRM 951 value of 4.05003 from Ishikawa and Terra (1997).⁸ All analytical data are in ESI Table S1.

4.2. Analysis of $\delta^7\text{Li}$ and $\delta^{11}\text{B}$ in basalts

We present the analytical results for standard basalt glasses and SRM 610, using SRM 612 as the bracketing standard by applying the optimised LA settings, with other analytical protocols being identical to the ones in Section 2. The net data acquisition time was only ~30 s, and the resultant signal intensities were typically ~20 mV ppm^{−1} for Li and ~7 mV ppm^{−1} for B in the case of samples containing several to several tens ppm of Li and B. These amounts were sufficient to obtain errors of 0.4–3‰ (2SE) from craters of 100 μm diameter and 40 μm depth (Table 2, all raw data are in ESI Table S2†).

Table 2 and Fig. 5a show $\delta^7\text{Li}$ analytical results for BCR-2G, BHVO-2G, JB-3 (groundmass), and GSD-1G basalt glasses, and SRM 610. The isotopic compositions of all basalt standards were highly heterogeneous for both synthetic glasses and natural groundmasses, at a spatial resolution of 100 μm. For example, BCR-2G showed $\delta^7\text{Li} = 4.07 \pm 4.70$ (2SD, *n* = 18), although the within-crater repeatability was less than ±1.5‰ (Fig. 5a). The same was true for the JB-2 groundmass and the GSD-1G synthetic glass formed by doping chemicals on a BCR-2 basaltic glass base (Fig. 5a).

Table 2 and Fig. 5b also show $\delta^{11}\text{B}$ analytical results for JB-2 (groundmass), BCR-2G, and GSD-1G basalt glasses, as well as SRM 610. The isotopic compositions of all basalt standards were, again, highly heterogeneous. The best example is provided by GSD-1G, which showed $\delta^{11}\text{B} = 10.5 \pm 1.9$ (2SD, *n* = 11) although the within-crater repeatability was less than ±0.5‰ 2SE (Fig. 5b).

4.3. Heterogeneity of standard materials

The above problems all originated from heterogeneities in the basalt glasses. ESI Fig. S1 and Table S3† show an example of a series of analyses conducted on GSD-1G using SRM 612 as the bracketing standard. The ¹⁰B/¹¹B values of SRM 612 varied within 2SE errors throughout the session (*n* = 20), whereas $\delta^{11}\text{B}$

of GSD-1G varied 10.5–12.2‰ with typical analytical errors of ±0.4‰ (2SE). The analytical values were constant in the first 11 spots, followed by the lowering of the values and a subsequent increase. The lowest two values were within the range of reference values of $\delta^{11}\text{B} = 9.8\text{--}10.75\text{‰}$.⁴ This suggests insufficient mixing of the chemicals and the base basalt, BCR-2, which shows $\delta^{11}\text{B} = -3.83 \pm 2.58\text{‰}$ (2SD, *n* = 10) (Table 2 and Fig. 5b).

A similar heterogeneity is observed for $\delta^7\text{Li}$ in GSD-1G, as shown in Fig. 5a. Previous GSD-1G results appeared to be homogeneous for B isotopes.¹⁹ However, the result contained analytical errors of ±3‰ (2SE), that masked local heterogeneity. The average value $\delta^{11}\text{B} = 12.41 \pm 1.94\text{‰}$ (2SD) was higher than that of the solution results $\delta^{11}\text{B} = 10.3 \pm 1.3\text{‰}$ (2SD) (Table 2).⁴ These basalt glass standards may be suitable for crater sizes of >500 × 1500 μm,^{16,20} but not for 100 μm or less. The use of such a heterogeneous standard is not recommended even when its matrix matches with other basalt glasses.

In contrast to the heterogeneous basalt glasses, the results of SRM 610 were almost perfectly reproducible for both $\delta^7\text{Li}$ and $\delta^{11}\text{B}$ (Fig. 5a and b). The analytical results were $\delta^7\text{Li} = 31.4 \pm 1.0\text{‰}$ (2SD, *n* = 3) and $\delta^{11}\text{B} = -0.33 \pm 0.28\text{‰}$ (2SD, *n* = 5), both reproducing the reference values of $\delta^7\text{Li} = 32.5 \pm 1.5\text{‰}$ and $\delta^{11}\text{B} = -0.52 \pm 0.53\text{‰}$,⁴ respectively (Table 2). It is encouraging that both the SRM 612 and SRM 610 glasses are highly homogeneous, such that they are suitable as external standards in sample-bracketing analyses.¹⁵

4.4. Quantitative basalt glass analysis with controlled ablation

The averaged analytical values obtained from various basalt standards and SRMs are plotted against their reference values in Fig. 6. Although the analytical errors (given by 2SD, Table 1, Fig. 4 and 5) are large compared with the analytical repeatability (2SE, Fig. 5), the averaged values all showed a one-to-one correspondence with the reference values (Fig. 6). Typical SIMS

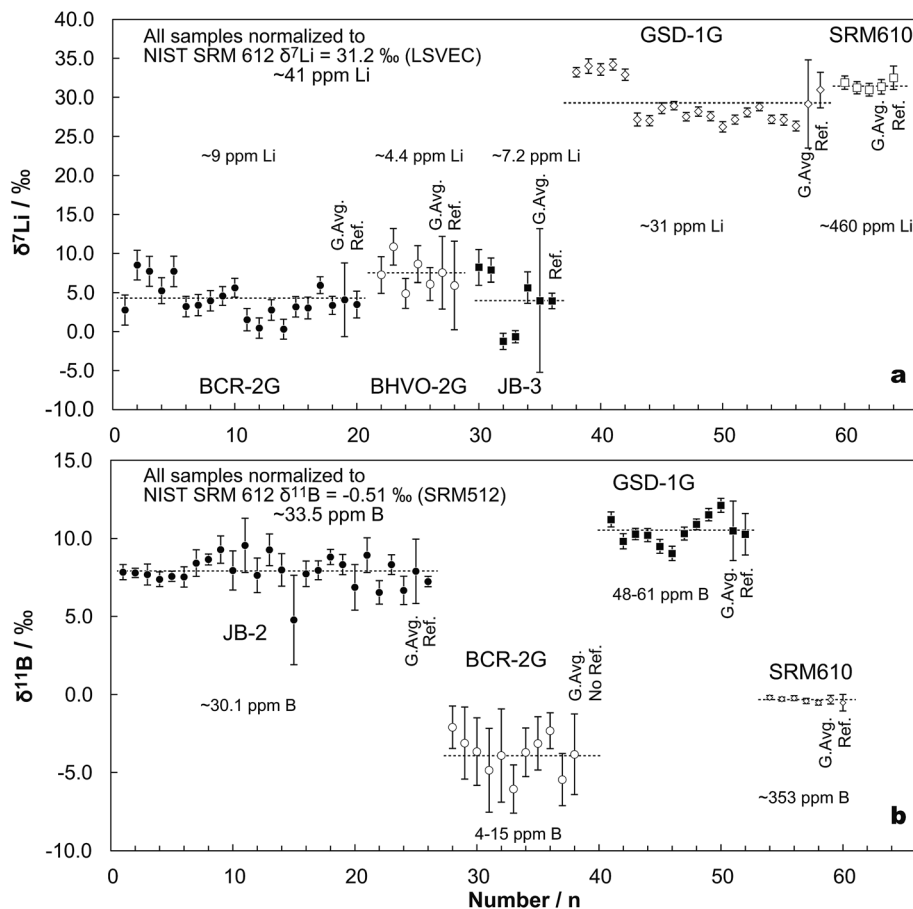


Fig. 5 Results of (a) Li and (b) B isotope ratio measurements in synthetic glasses and basalt groundmass analysed using NIST SRM 612 as a bracketing standard. Isotope ratios were recalculated by normalisation with respect to SRM 8445 for Li and NIST SRM 951 for B. The LA conditions used were a 100 μm diameter \times 40 μm deep crater with a 100–120 mJ 193 nm ArF laser operating at 5 Hz. The typical drilling rate was $\sim 0.3 \mu\text{m}$ per shot. Data acquisition comprised 50 scans of ~ 0.5 s. Gas blanks were measured before and after sample ablation. Note that all but GSD-1 and NIST SRM 610 and 612 glasses were heterogeneous, requiring large numbers of analytical spots to obtain the average reference values. These average values agreed well (within $<1\text{‰}$) with the reference values. GSD-1 G showed slightly higher ($>1\text{--}1.5\text{‰}$) isotope ratios for both B and Li. These results confirmed the repeatability of the analyses for different matrices at a $<1\text{‰}$ level.

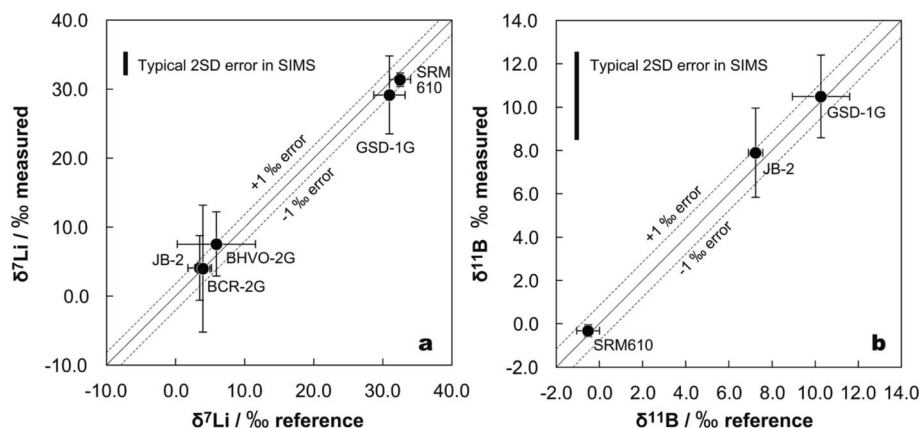


Fig. 6 Correlations between reference and measured values of the standard reference samples for (a) Li and (b) B isotopes. The reference and measured values agreed well within analytical uncertainties. Errors are 2SD for both reference and measured values (see source data in Fig. 2). Typical analytical errors in SIMS are shown for comparison (Kobayashi *et al.*, 2004). Typical LA-MC-ICPMS 2SD errors in a spot were $\sim 1\text{--}2\text{‰}$ for 10–30 ppm Li/B samples (see Table 1), whereas the large heterogeneity of standard rocks and glasses increased the apparent analytical errors (see Fig. 2). Nevertheless, a one-to-one correlation of average values with the reference values was obtained.

analytical errors for both Li and B isotopes are shown for comparison, and the ranges were calculated from analytical errors in standard glasses by Kobayashi *et al.* (2004).¹² The diagrams show that the averaged values were within $\pm 1.0\%$ of the reference values for both $\delta^7\text{Li}$ and $\delta^{11}\text{B}$. Therefore, the laboratory bias for ablation-optimised 193ExLA was typically better than $\pm 1.0\%$, with an analytical repeatability of $\pm 0.5\%$ achieved for samples containing several tens of ppm of Li and B, and $\pm 2\text{--}3\%$ for samples containing several ppm of these elements.

5. Isotope compositions of minerals with different matrices

We have shown that controlled ablation using 193ExLA enabled accurate analyses of basalt glasses using SRM 612 as a standard. This indicates that the matrix effects in these glasses are almost negligible under these conditions. Thermal fractionation in the 193ExLA site was also trivial. The drawback of this method is its non-applicability to crater diameters of less than 50 μm (Fig. 2).¹⁵ The low laser fluence in commercially available 193ExLA systems^{15,18,19} may also be a problem, and applying this method to extremely different matrices can lead to a large analytical bias.^{18,20} To cope with these problems, we herein propose a new analytical protocol applicable to a wide range of samples.

5.1. Ablation volume correction (AVC) analytical protocol

As discussed above, isotopic fractionation mainly depends on the amount of sample loaded to the ICP. Controlled ablation is useful for glass samples with different matrices due to the quasi-constant ablation volume. These results support the validity of using ablation volume to correct for laser parameter-induced fractionation. We herein propose an ablation volume correction (AVC) analytical protocol. This method is particularly useful for samples with matrices extremely different from that of the SRM 61X standard. We know that extremely Fe-rich materials, such as pyroxenes, are more effectively ablated than SRM 61X glass (at $\sim 110\%$).³¹ The volatile-rich phosphate mineral apatite is ablated even more efficiently (at $>200\%$).³² Conversely, Fe-poor minerals, such as plagioclase, are less ablated than SRM 61X (at $\sim 60\%$).³⁹ This discrepancy is largely due to the thermal conductivity of these materials.³¹

We measured the ablated crater volume using a VHS-5000 digital microscope (Keyence Co., Osaka, Japan). We first analysed $\delta^7\text{Li}$ and $\delta^{11}\text{B}$ for SRM 612 with different laser repetition rates of 1, 3, 5, 7, 10, 15, and 20 Hz at the same crater diameter of 100 μm and plotted their values against the signal intensities (V) and ablated volumes (μm^3) (Fig. 7 and ESI Table S4†), which showed linear correlations for both Li and B isotopes, indicating the versatility of the volume correction method. The linear correlation, however, was disrupted at 1 and 3 Hz for $\delta^7\text{Li}$ due to the dominant axial fractionation; in contrast, $\delta^{11}\text{B}$ exhibited an almost linear correlation under all conditions (Fig. 3, see also Lin *et al.*, 2014 for axial fractionation of B isotopes).¹⁹ These relationships appear to be inconsistent with

the aforementioned results that showed a linear correlation for $\delta^7\text{Li}$ but a curvilinear correlation for $\delta^{11}\text{B}$ (Fig. 2a and b). This discrepancy is likely due to the inter-day variance of the instrumental settings, such as the sample gas flow rate that controls axial plasma positioning in the ICP (Fig. 3).¹⁹

Overall, linear relationships were maintained for >5 Hz ablation conditions. Otherwise, curve fitting can account for the non-linear fractionation regions as long as the instrumental conditions are consistent, as exemplified by the two sets of measurements made in 4 h (Fig. 7 and ESI Table S4†). The overall performance of AVC is $<1\%$ larger or comparable with the typical 2SE errors of $\pm 0.4\text{--}0.7\%$ obtained for 100 μm craters with several tens of ppm of Li and B.

5.2. Analyses of $\delta^7\text{Li}$ in jadeite and $\delta^{11}\text{B}$ in tourmaline crystals by AVC

We explored the applicability of the AVC analytical protocol for jadeite and tourmaline minerals to determine $\delta^7\text{Li}$ and $\delta^{11}\text{B}$, respectively. The purpose of these experiments was to confirm the versatility of the above protocol for non-matrix-matched minerals using SRM 61X as a standard.

Prior to the application of the above method, $\delta^7\text{Li}$ and $\delta^{11}\text{B}$ compositions of these minerals were determined using the bulk analysis methods described previously, *i.e.*, Neptune solution MFC-ICPMS^{60,61} for $\delta^7\text{Li}$ and the same MFC-ICPMS⁶²⁻⁶⁴ for $\delta^{11}\text{B}$ at the Kochi Institute of Core Sample Research of JAMSTEC. Mineral samples of sizes >6 cm^2 and 4 mm thick were broken into three pieces, and the central portion was crushed with an alumina pestle; these pieces were used for bulk analyses. The remaining fragments were used for LA-MFC-ICPMS analyses.

We used 100 and 50 μm craters at 10 and 3 Hz laser repetition rates for jadeite and tourmaline, respectively. A reduced laser fluence of ~ 12 J cm^{-2} was used throughout (Table 1, ESI Tables S5 and S6†). The purpose of this ablation condition was twofold: matching the Li and B signal intensities with the optimal analytical range of LA-MFC-ICPMS, and matching the conditions with the commercially available ordinal 193ExLA systems. The results are given in Table 3, together with the measured crater volumes of the SRM 612 standard and of the jadeite and tourmaline minerals.

Fig. 8 shows the results of the AVC protocol and corrected $\delta^7\text{Li}$ values compared to the bulk TIMS results for jadeite (ESI Table S5†). The AVC corrections were made using the relationship between the crater volume and the measured $\delta^7\text{Li}$ value for SRM 612. The crater volumes of jadeite were consistently *ca.* half of those for SRM 612 at 10 Hz, which was equivalent to the 5 Hz ablation volume of SRM 612. The result was a -0.3% shift for jadeite (Fig. 8a), obtained using the relationship for the correction of jadeite spots (Fig. 8b). The volume-corrected $\delta^7\text{Li}$ in jadeite showed a wide variation, ranging from *ca.* -10 to *ca.* 0% . The $\delta^7\text{Li}$ values positively correlated with Li concentrations, indicating binary mixing between a low Li concentration-light $\delta^7\text{Li}$ source and a high Li concentration-heavy $\delta^7\text{Li}$ isotope source (Fig. 8c). Considering this stoichiometric relationship, the average LA value is $\delta^7\text{Li} = 1.3 \pm 3.3\%$ (2SD) at a Li concentration of 25 ppm. This is fully consistent with the bulk

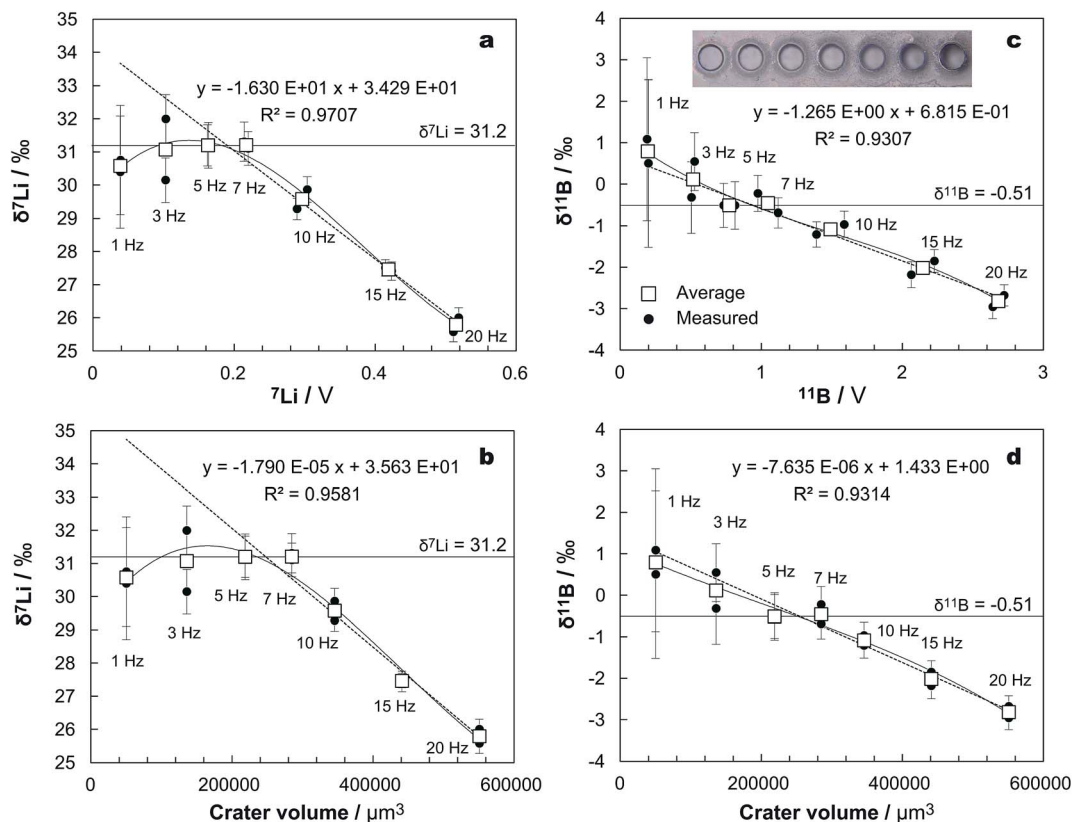


Fig. 7 Correlation between isotopic fractionation, signal intensity, and ablated crater volume. Panels (a) and (b) represent data for $\delta^7\text{Li}$, while panels (c) and (d) represent data for $\delta^{11}\text{B}$. Linear regressions are applicable for 5–20 Hz and 1–20 Hz ablations for Li and B isotopes, respectively. Note that ablation volume correction is possible even if the Li and B concentrations of a sample are unknown. Curved regression lines were obtained by third-order polynomial fittings. All isotope ratios were normalised to 5 Hz results corresponding to the reference values.

Table 3 Li and B isotope compositions for jadeite and tourmaline samples^a

Sample	$\delta^7\text{Li}$ relative to SRM 8545	$\delta^{11}\text{B}$ relative to SRM 951
Solution	Low-T Jadeite	Tourmaline
Conc. (ppm)	$+1.32 \pm 0.34$ ($n = 6$)	-7.49 ± 0.25 ($n = 6$)
LA-MFC-ICP	24.9 ± 3.1	$30\,000 \pm 5300$
	$+1.3 \pm 3.3$ ($n = 13$) at 25 ppm Li	-8.1 ± 0.4 ($n = 15$) at 30 000 ppm B

^a Results and errors are given in ‰. Errors for solution are given in 2SE, others are 2SD. SRM 8545 value of 12.17 from Kasemann *et al.* (2005).³⁵ SRM 951 value of 4.05003 from Ishikawa and Terra (1997).⁸ Isotope ratios by LA-MFC-ICPMS are normalised to SRM 612 by the ablation volume correction method (see text). All analytical data are in ESI Tables S5 and S6. Standard analyses of JB-2 yielded $\delta^7\text{Li} = 6.90 \pm 0.38\text{‰}$ for $6.81 \pm 0.21\text{‰}$ and $\delta^{11}\text{B} = 4.34 \pm 0.13\text{‰}$ for $4.45 \pm 0.24\text{‰}$ consistent with the literature values.^{9,63} See the text for the methods of solution analyses.

$\delta^7\text{Li}$ value of $1.32 \pm 0.34\text{‰}$ for 24.9 ppm Li (open star in Fig. 8c and Table 3).

Fig. 9 shows the results of AVC measurements and AVC-ed $\delta^{11}\text{B}$ values in comparison to those obtained by bulk MFC-ICPMS for the tourmaline crystal (ESI Table S6†). Due to the high concentration of B in tourmaline ($\sim 30\,000$ ppm), small 50 μm craters were used with a lower repetition rate of 3 Hz. The standard was also altered from SRM 612 to SRM 610 (~ 350 ppm B) to match the intensity range of the small crater. AVC calibration was performed using 50 μm craters (Fig. 9a). The ablated crater volumes of tourmaline were *ca.* half of those for SRM 610, being similar to those of jadeite. The uncorrected $\delta^{11}\text{B}$ values were systematically lower (Fig. 9b). The AVC-ed value was

$\delta^{11}\text{B} = -8.4 \pm 0.5\text{‰}$ (2SD) on average, whereas that for 30 000 ppm B was $-8.1 \pm 0.4\text{‰}$, consistent with that of the bulk at $-7.49 \pm 0.25\text{‰}$ at 30 000 ppm B (open star in Fig. 9c and Table 3).

The above results obviate the versatility of the AVC analytical protocol that assures both the repeatability and the laboratory bias of better than $\pm 0.2\text{‰}$ for $\delta^7\text{Li}$ and $\pm 0.7\text{‰}$ for $\delta^{11}\text{B}$ in matrix-unmatched jadeite and tourmaline, respectively.

5.3. Summary of the AVC analytical protocol

(1) Unknown samples are first analysed by LA-MFC-ICPMS to obtain an approximate Li/B concentration to obtain the

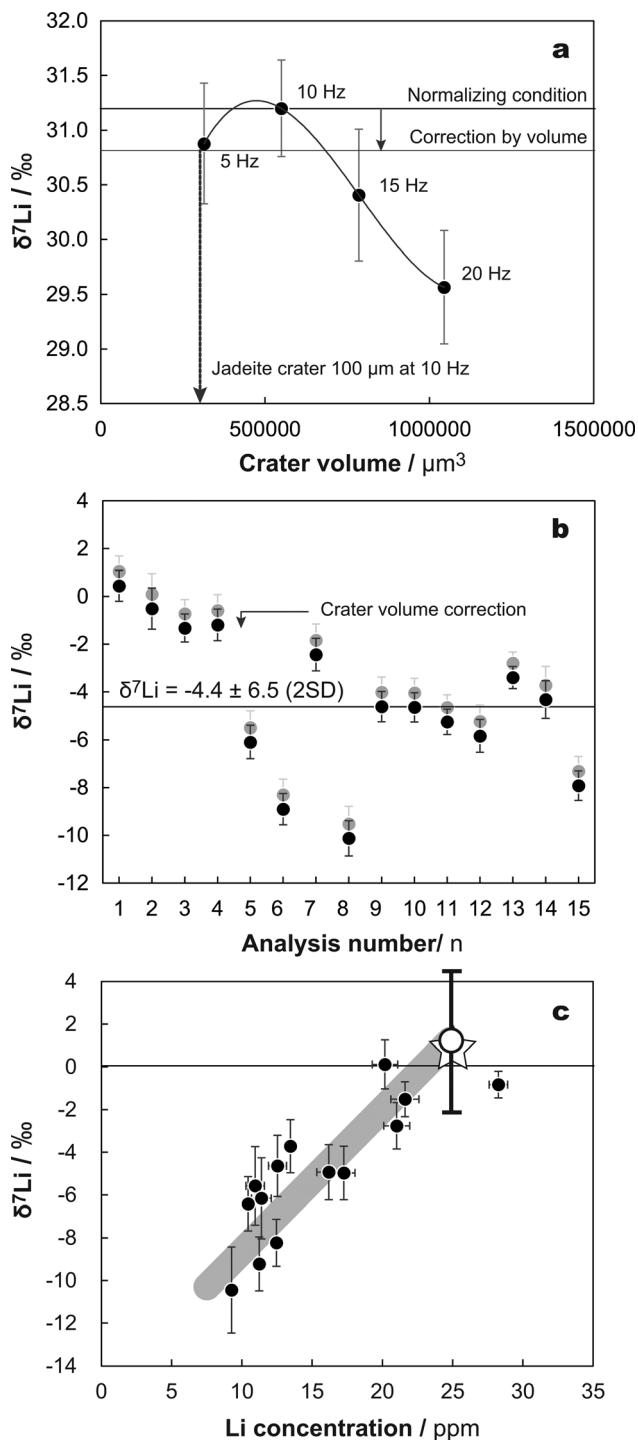


Fig. 8 Plot of Li isotope ratios vs. ablation volume for SRM 612 glass (a), crater volume-uncorrected and -corrected Li isotope ratios of jadeites (b), and Li concentrations in jadeites (panel c). The open star (c) shows the average value of bulk analysis.

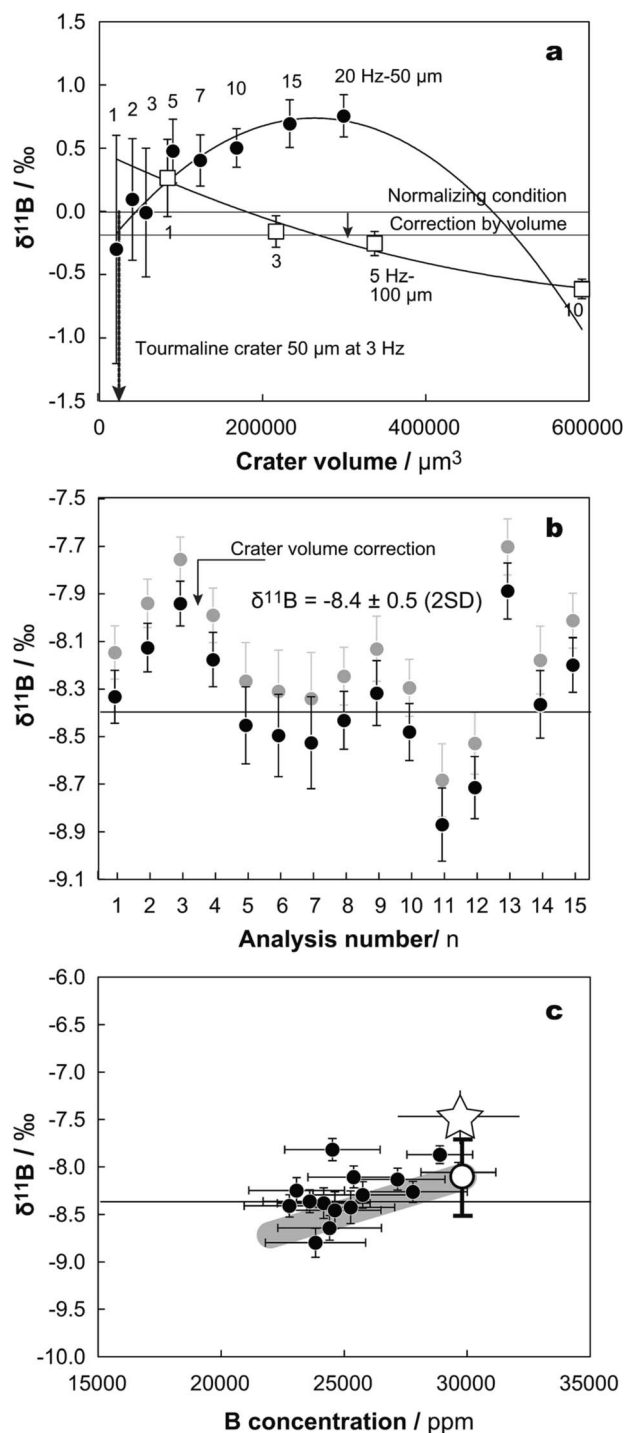


Fig. 9 Plot of B isotope ratios vs. ablation volume for SRM 610 glass (a), crater volume-uncorrected and -corrected B isotope ratios of jadeites (b), and B concentrations in jadeites (panel c). Open star (c) shows the average value of bulk analysis with errors.

required sample volume, which determines the crater diameter and the approximate LA repetition rate. Ablation of SRM 61X is needed for comparison.

(2) A proper standard (SRM 610/612) is chosen for the bracketing standard. The signal intensities should be sufficient for the required precision of this standard.

(3) Analysis of $\delta^7\text{Li}/\delta^{11}\text{B}$ and the signal intensity of $^7\text{Li}/^{11}\text{B}$ (V) for SRM 61X are carried out with the determined crater diameter at different LA repetition rates. The resultant crater volumes should cover the crater volume dug on unknown samples.

(4) The volume is accurately measured for all SRM 61X craters using a microscope (e.g., digital microscope).

(5) The correlation between crater volumes $V(x)$ and the $\delta^7\text{Li}(y)$ or $\delta^{11}\text{B}(y)$ isotope ratios is calculated as in Fig. 8a and 9a.

(6) The unknowns and bracketing standards are analysed at the given crater diameter and LA repetition rate.

(7) All crater volumes of unknown samples are accurately measured using a microscope (e.g., digital microscope). One assumes that the crater volumes of SRM 61X are constant and equal to those measured in (4).

(8) The isotope ratios of the unknown samples are recalculated using $V(x)$ versus $\Delta\delta^7\text{Li}(y)$ or $\Delta\delta^{11}\text{B}(y)$ correlations, as in Fig. 8a and 9a.

This AVC protocol is commonly applicable to all analytical facilities and a wide range of unknown samples. The use of a cylindrical crater with a flat bottom helps to measure the crater volumes accurately, which is crucial for this method (Fig. 7). As shown, neither the ICP setup, nor interface cones and LA optimisation can properly eliminate the ICP-induced isotopic fractionation when samples with different matrices are analysed.^{19,24} The developed AVC protocol is useful in accounting for these issues until an extremely robust ICP method is developed.

6. Conclusions

We examined laser ablation parameters and the origin of isotopic fractionation in LA-MFC-ICPMS for $\delta^7\text{Li}$ and $\delta^{11}\text{B}$ analyses of basalt glasses and minerals, using SRM 61X glasses as standards. Both 193ExLA and 266FsLA were tested at various ablation parameters, including different crater diameters and laser repetition rates at given laser fluences. The main mechanism for isotopic fractionation was ascribed to the effect of ICP mass loading, which resulted in a lowered plasma temperature and Rayleigh fractionation of lighter isotopes during dissociation of the laser particles in the plasma. The subordinate fractionation mechanism also was deduced to be Rayleigh fractionation at the molten crater walls and the thermal effect. The latter effect was more enhanced for 193ExLA than for 266FsLA, but the former effect was dominant. Controllable ablation with 193ExLA was more important for reducing the fractionation between SRM 61X standards and unknown basalts. The use of constant ablation with a $100 \times 40 \mu\text{m}$ crater at a constant repetition rate of 5 Hz and a fluence of $\sim 20 \text{ J cm}^{-2}$ allowed quantitative analyses of basalt glasses using the SRM 612 glass as a standard. For samples with significantly different matrices, we finally propose an ablation volume correction (AVC) analytical protocol. Due to the calibration curve established using the relationship between crater volume and isotopic fractionation, both the repeatability and laboratory bias were within $\pm 1\%$ (2SD) in both $\delta^7\text{Li}$ and $\delta^{11}\text{B}$ analyses. Application of the AVC method to Li isotopes in a jadeite crystal and to B isotopes in a tourmaline crystal enabled precise and reproducible *in situ* analyses, using SRM 612 and 610 glasses as standards, respectively. This new AVC method is applicable to any LA-MFC-ICPMS instruments, as long as an accurate measurement of crater volume is possible.

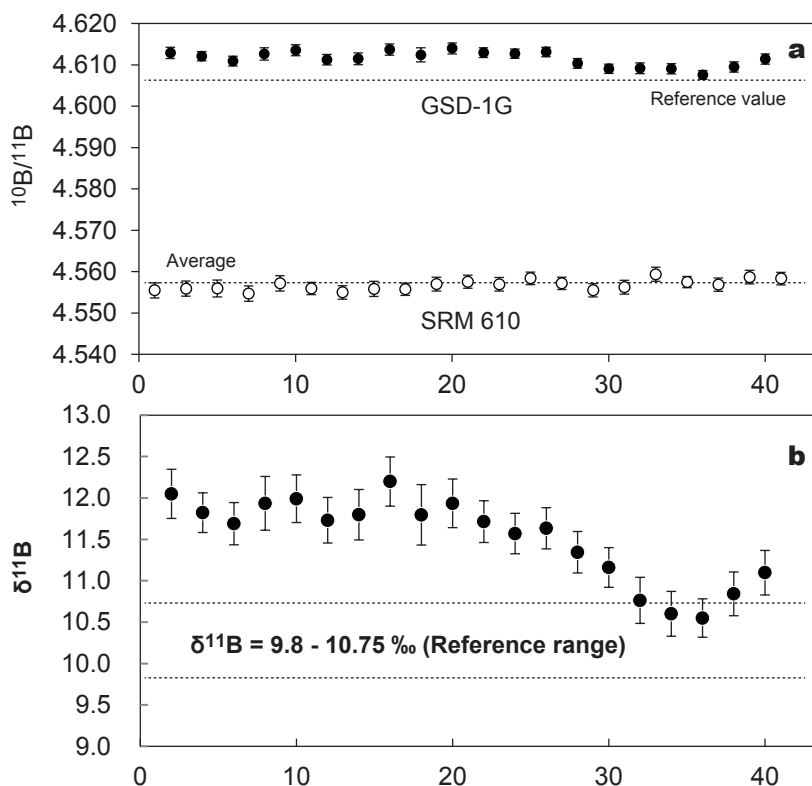
Acknowledgements

We thank Prof. T. Hirata of the University of Tokyo and Dr K. Nagaishi of the Kochi Institute of Core Sample Research. T. T. thanks K. Azami for sharing tourmaline crystals from his private collection. Comments from two anonymous reviewers helped us to improve the clarity of this paper. J.-I. K. and T. I. were funded by JSPS grants 15H02148 and 16H04066, respectively.

References

- 1 H. S. Peiser, N. E. Holden, P. De Bièvre, I. L. Barnes, R. Hagemann, J. R. De Laeter, T. J. Murphy, E. Roth, M. Shima and H. G. Thode, *Pure Appl. Chem.*, 1984, **56**, 965–968.
- 2 S. Barth, *Geol. Rundsch.*, 1993, **82**, 640–651, DOI: 10.1007/bf00191491.
- 3 B. Wunder, A. Mexiner, R. L. Romer and W. Heinrich, *Contrib. Mineral. Petrol.*, 2005, **151**, 112–120, DOI: 10.1007/s00410-005-0049-0.
- 4 W. A. Brand, T. B. Coplen, J. Vogl, M. Rosner and T. Prohaska, *Pure Appl. Chem.*, 2014, **86**, 425–467, DOI: 10.1515/pac-2013-1023.
- 5 H. R. Marschall, R. Altherr and L. Rüpke, *Chem. Geol.*, 2007, **239**, 323–335, DOI: 10.1016/j.chemgeo.2006.08.008.
- 6 H. R. Marschall, A. V. Korsakov, G. L. Luvizotto, L. Nasdala and T. Ludwig, *J. Geol. Soc.*, 2009, **166**, 811–823, DOI: 10.1144/0016-76492008-042.
- 7 H. R. Marschall, P. A. E. Pogge von Strandmann, H.-M. Seitz, T. Elliott and Y. Niu, *Earth Planet. Sci. Lett.*, 2007, **262**, 563–580, DOI: 10.1016/j.epsl.2007.08.005.
- 8 T. Ishikawa and F. Tera, *Earth Planet. Sci. Lett.*, 1997, **152**, 123–138, DOI: 10.1016/S0012-821X(97)00144-1.
- 9 T. Moriguti and E. Nakamura, *Earth Planet. Sci. Lett.*, 1998, **163**, 167–174, DOI: 10.1016/S0012-821X(98)00184-8.
- 10 R. L. Rudnick and D. A. Ionov, *Earth Planet. Sci. Lett.*, 2007, **256**, 278–293, DOI: 10.1016/j.epsl.2007.01.035.
- 11 G. F. Davies, *Geochem., Geophys., Geosyst.*, 2009, **10**, DOI: 10.1029/2009gc002634.
- 12 K. Kobayashi, R. Tanaka, T. Moriguti, K. Shimizu and E. Nakamura, *Chem. Geol.*, 2004, **212**, 143–161, DOI: 10.1016/j.chemgeo.2004.08.050.
- 13 T. Nakano and E. Nakamura, *Phys. Earth Planet. Inter.*, 2001, **127**, 233–252, DOI: 10.1016/S0031-9201(01)00230-8.
- 14 G. E. Bebout, P. Agard, K. Kobayashi, T. Moriguti and E. Nakamura, *Chem. Geol.*, 2013, **342**, 1–20, DOI: 10.1016/j.chemgeo.2013.01.009.
- 15 C. Martin, E. Ponzevera and G. Harlow, *Chem. Geol.*, 2015, **412**, 107–116, DOI: 10.1016/j.chemgeo.2015.07.022.
- 16 P. J. le Roux, S. B. Shirey, L. Benton, E. H. Hauri and T. D. Mock, *Chem. Geol.*, 2004, **203**, 123–138, DOI: 10.1016/j.chemgeo.2003.09.006.
- 17 M. Tiepolo, C. Bouman, R. Vannucci and J. Schwieters, *Appl. Geochem.*, 2006, **21**, 788–801, DOI: 10.1016/j.apgeochem.2006.02.014.
- 18 J. Miková, J. Kosler and M. Wiedenbeck, *J. Anal. At. Spectrom.*, 2014, **29**, 903–914, DOI: 10.1039/c3ja50241d.

- 19 L. Lin, Z. Hu, L. Yang, W. Zhang, Y. Liu, S. Gao and S. Hu, *Chem. Geol.*, 2014, **386**, 22–30, DOI: 10.1016/j.chemgeo.2014.08.001.
- 20 P. J. le Roux, *J. Anal. At. Spectrom.*, 2010, **25**, 1033–1038, DOI: 10.1039/b920341a.
- 21 J.-I. Kimura, H. Kawabata, Q. Chang, T. Miyazaki and T. Hanyu, *Geochem. J.*, 2013, **47**, 369–384.
- 22 J.-I. Kimura, Q. Chang, N. Kanazawa, S. Sasaki and B. S. Vaglarov, *J. Anal. At. Spectrom.*, 2016, **31**, 790–800, DOI: 10.1039/c5ja00374a.
- 23 J. Kosler, R. B. Pedersen, C. Kruber and P. J. Sylvester, *J. Anal. At. Spectrom.*, 2005, **20**, 192–199, DOI: 10.1039/b412169d.
- 24 S. E. Jackson and D. Günther, *J. Anal. At. Spectrom.*, 2003, **18**, 205–212, DOI: 10.1039/b209620j.
- 25 H.-R. Kuhn, N. J. Pearson and S. E. Jackson, *J. Anal. At. Spectrom.*, 2007, **22**, 547–552, DOI: 10.1039/b616232k.
- 26 K. Ikehata, K. Notsu and T. Hirata, *J. Anal. At. Spectrom.*, 2008, **23**, 1003–1008, DOI: 10.1039/b801044g.
- 27 I. Horn, F. von Blanckenburg, R. Schoenberg, G. Steinhoefel and G. Markl, *Geochim. Cosmochim. Acta*, 2006, **70**, 3677–3688, DOI: 10.1016/j.gca.2006.05.002.
- 28 R. G. Coleman, *J. Petrol.*, 1961, **2**, 209–247, DOI: 10.1093/petrology/2.2.209.
- 29 T. Tsujimori, J. G. Liou and R. G. Coleman, in *Convergent Margin Terranes and Associated Regions: a Tribute to W.G. Ernst*, ed. M. Cloos, W. D. Carlson, M. C. Gilbert, J. G. Liou and S. S. Sorensen, Geological Society of America Special Publication, 2007, vol. 419, pp. 67–80.
- 30 S. Kondo, *Jpn. Assoc. Mineral., Petrol. Econ. Geol.*, 1953, **37**, 148–155.
- 31 J.-I. Kimura and Q. Chang, *J. Anal. At. Spectrom.*, 2012, **27**, 1549–1559, DOI: 10.1039/c2ja10344c.
- 32 J.-I. Kimura, Q. Chang and H. Kawabata, *J. Anal. At. Spectrom.*, 2013, **28**, 1522–1529, DOI: 10.1039/c3ja50109d.
- 33 S. M. Eggins, L. P. J. Kinsley and J. M. G. Shelley, *Appl. Surf. Sci.*, 1998, **127–129**, 278–286, DOI: 10.1016/s0169-4332(97)00643-0.
- 34 C. Bouman, M. Deerberg and J. B. Schwieters, *Application Note Thermo Scientific*, 2009, vol. 30187, pp. 1–4.
- 35 S. A. Kasemann, A. B. Jeffcoate and T. Elliott, *Anal. Chem.*, 2005, **77**, 5251–5257, DOI: 10.1021/ac048178h.
- 36 K. P. Jochum and B. Stoll, in *Current Practices and Outstanding Issues, Laser Ablation ICP-MS in the Earth Sciences*, Mineralogical Association of Canada, Vancouver, 2008, vol. 40, pp. 147–168.
- 37 J. Fietzke, A. Heinemann, I. Taubner, F. Bohm, J. Erez and A. Eisenhauer, *J. Anal. At. Spectrom.*, 2010, **25**, 1953–1957, DOI: 10.1039/c0ja00036a.
- 38 G. D. Flesch, A. R. Anderson and H. J. Svec, *Int. J. Mass Spectrom. Ion Phys.*, 1973, **12**, 265–272, DOI: 10.1016/0020-7381(73)80043-9.
- 39 E. J. Catanzaro, National Bureau of Standards, Institute for Materials Research, 1970, 17.
- 40 J.-I. Kimura, Q. Chang and K. Tani, *Geochem. J.*, 2011, **45**, 283–296.
- 41 S. R. Houk, K. R. Winge and C. Xiaoshan, *J. Anal. At. Spectrom.*, 1997, **12**, 1139–1148, DOI: 10.1039/a607579g.
- 42 H. Andren, I. Rodushkin, A. Stenberg, D. Malinovsky and D. C. Baxter, *J. Anal. At. Spectrom.*, 2004, **19**, 1217–1224, DOI: 10.1039/b403938f.
- 43 A. Montaser, *Inductively Coupled Plasma Mass Spectrometry*, Wiley-VCH, New York, 1998.
- 44 I. I. Stewart and J. W. Olesik, *J. Am. Soc. Mass Spectrom.*, 1999, **10**, 159–174, DOI: 10.1016/S1044-0305(98)00136-6.
- 45 F. Vanhaecke, R. Dams and C. Vandecasteele, *J. Anal. At. Spectrom.*, 1993, **8**, 433–438, DOI: 10.1039/ja9930800433.
- 46 M. Aghaei and A. Bogaerts, *J. Anal. At. Spectrom.*, 2016, **31**, 631–641, DOI: 10.1039/c5ja00162e.
- 47 F.-X. D'Abzac, A.-M. Seydoux-Guillaume, J. Chmeleff, L. Datas and F. Poitrasson, *J. Anal. At. Spectrom.*, 2012, **27**, 108–119, DOI: 10.1039/c1ja10145d.
- 48 J. J. Gonzalez, C. Liu, S.-B. Wen, X. Mao and R. E. Russo, *Talanta*, 2007, **73**, 567–576, DOI: 10.1016/j.talanta.2007.1004.1029.
- 49 J. J. Gonzalez, C. Liu, S.-B. Wen, X. Mao and R. E. Russo, *Talanta*, 2007, **73**, 577–582, DOI: 10.1016/j.talanta.2007.1004.1028.
- 50 F. Poitrasson, X. Mao, S. S. Mao, R. Freyrier and R. E. Russo, *Anal. Chem.*, 2003, **75**, 6184–6190.
- 51 B. Fernández, F. Claverie, C. Pécheyran and O. F. X. Donald, *Trends Anal. Chem.*, 2007, **26**, 951–966, DOI: 10.1016/j.trac.2007.1008.1008.
- 52 I. Horn, R. L. Rudnick and W. F. McDonough, *Chem. Geol.*, 2000, **164**, 281–301.
- 53 I. Krosiakova and D. Günther, *J. Anal. At. Spectrom.*, 2007, **22**, 51–62.
- 54 Z.-C. Yan and G. W. F. Drake, *Phys. Rev. A*, 1995, **52**, 3711–3717, DOI: 10.1103/PhysRevA.52.3711.
- 55 B. Edlén, A. Ölme, G. Herzberg and J. W. C. Johns, *J. Opt. Soc. Am.*, 1970, **60**, 889–891, DOI: 10.1364/josa.60.000889.
- 56 G. Horlick and Y. Shao, in *Inductively Coupled Plasma in Analytical Atomic Spectrometry*, ed. A. Montaser and D. W. Golightly, VCH Pub. Inc., New York, 2nd edn, 1992, p. 564.
- 57 K. Newman, *J. Anal. At. Spectrom.*, 2011, **27**, 63–70, DOI: 10.1039/c1ja10222b.
- 58 K. Newman, P. A. Freedman, J. Williams, N. S. Belshaw and A. N. Halliday, *J. Anal. At. Spectrom.*, 2009, **24**, 742–751.
- 59 J.-I. Kimura, T. Takahashi and Q. Chang, *J. Anal. At. Spectrom.*, 2013, **28**, 945–957, DOI: 10.1039/c3ja30329b.
- 60 Y. Nishio, A. Ijiri, T. Toki, Y. Morono, M. Tanimizu, K. Nagaishi and F. Inagaki, *Earth Planet. Sci. Lett.*, 2015, **414**, 144–155, DOI: 10.1016/j.epsl.2015.01.018.
- 61 Y. Nishio, K. Okamura, M. Tanimizu, T. Ishikawa and Y. Sano, *Earth Planet. Sci. Lett.*, 2010, **297**, 567–576, DOI: 10.1016/j.epsl.2010.07.008.
- 62 K. Yamaoka, T. Ishikawa, O. Matsubaya, D. Ishiyama, K. Nagaishi, Y. Hiroyasu, H. Chiba and H. Kawahata, *Geochim. Cosmochim. Acta*, 2012, **84**, 543–559, DOI: 10.1016/j.gca.2012.01.043.
- 63 T. Ishikawa and K. Nagaishi, *J. Anal. At. Spectrom.*, 2011, **26**, 359–365, DOI: 10.1039/c0ja00060d.
- 64 G. L. Foster, *Earth Planet. Sci. Lett.*, 2008, **271**, 254–266, DOI: 10.1016/j.epsl.2008.04.015.
- 65 K. P. Jochum, U. Nohl, K. Herwig, E. Lammel, B. Stoll and A. W. Hofmann, *Geostand. Geoanal. Res.*, 2005, **29**, 333–338.



ESI Figure S1: Heterogeneity of the GSD-1G glass used for B isotope ratio determination. The raw B isotope ratios are shown for SRM 612 as the bracketing standard and GSD-1G as the bracketed unknown (a). NIST SRM 951 normalised isotope ratios show significant spatial variation compared with the reference analytical results from the bulk GSD-1G sample (b). In contrast, SRM 612 has a fairly uniform composition with deviations within an uncertainty of $< 0.5\text{‰}$, indicating its suitability for use as a bracketing standard (see (a)). All errors are 2SD.

ESI Table S1. Analytical results of SRM 612 glass with different ablation parameters^a

Ablation condition	Sample	⁶ Li / V	2SE	⁷ Li / V	2SE	⁷ Li/ ⁶ Li	2SE	δ ⁷ Li	2SE
30um/10Hz/193nm	SRM612_1	0.0107	0.0003	0.1654	0.0047	15.442	0.025	39.1	1.6
30um/20Hz/193nm	SRM612_2	0.0165	0.0009	0.2555	0.0140	15.468	0.021	40.2	1.4
50um/2Hz/193nm	SRM612_3	0.0069	0.0001	0.1069	0.0021	15.392	0.035	35.7	2.3
50um/5Hz/193nm	SRM612_4	0.0151	0.0001	0.2320	0.0021	15.401	0.019	36.6	1.2
50um/10Hz/193nm	SRM612_5	0.0269	0.0004	0.4151	0.0061	15.416	0.011	37.6	0.7
50um/20Hz/193nm	SRM612_6	0.0452	0.0014	0.6962	0.0208	15.395	0.008	36.2	0.5
100um/1Hz/193nm	SRM612_7	0.0130	0.0002	0.1991	0.0034	15.368	0.024	33.1	1.5
100um/2Hz/193nm	SRM612_8	0.0237	0.0005	0.3641	0.0072	15.358	0.013	32.6	0.9
100um/5Hz/193nm	SRM612_9	0.0589	0.0009	0.9037	0.0131	15.338	0.006	31.2	0.4
100um/10Hz/193nm	SRM612_10	0.0864	0.0006	1.3228	0.0098	15.313	0.005	29.8	0.3
100um/20Hz/193nm	SRM612_11	0.1591	0.0025	2.4284	0.0378	15.262	0.003	26.7	0.2
200um/1Hz/193nm	SRM612_12	0.0372	0.0005	0.5701	0.0082	15.317	0.010	29.9	0.6
200um/2Hz/193nm	SRM612_13	0.0683	0.0008	1.0437	0.0119	15.276	0.007	27.5	0.5
200um/5Hz/193nm	SRM612_14	0.1502	0.0018	2.2859	0.0270	15.219	0.004	23.6	0.3

^a: 2SE: 2-standard error

Ablation condition	Sample	⁶ Li / V	2SE	⁷ Li / V	2SE	⁷ Li/ ⁶ Li	2SE	δ ⁷ Li	2SE
30um/10Hz/266nm	SRM612_1	0.0019	0.0001	0.0292	0.0012	15.695	0.139	44.9	8.8
30um/20Hz/266nm	SRM612_2	0.0069	0.0002	0.1071	0.0035	15.510	0.059	32.9	3.8
30um/30Hz/266nm	SRM612_3	0.0110	0.0009	0.1712	0.0136	15.536	0.030	34.6	1.9
50um/20Hz/266nm	SRM612_4	0.0050	0.0002	0.0780	0.0024	15.604	0.045	39.0	2.9
50um/30Hz/266nm	SRM612_5	0.0253	0.0008	0.3922	0.0129	15.517	0.014	33.3	0.9
50um/60Hz/266nm	SRM612_6	0.0306	0.0029	0.4750	0.0455	15.537	0.016	34.6	1.0
100um/10Hz/266nm	SRM612_7	0.0115	0.0002	0.1783	0.0038	15.490	0.027	31.6	1.7
100um/10Hz/266nm	SRM612_8	0.0090	0.0002	0.1402	0.0032	15.548	0.026	35.4	1.7
100um/20Hz/266nm	SRM612_9	0.0223	0.0003	0.3466	0.0051	15.517	0.016	33.4	1.0
100um/30Hz/266nm	SRM612_10	0.0570	0.0016	0.8829	0.0244	15.484	0.007	31.2	0.5
100um/30Hz/266nm	SRM612_11	0.0493	0.0009	0.7635	0.0141	15.485	0.007	31.3	0.5
100um/30Hz/266nm	SRM612_12	0.0472	0.0012	0.7310	0.0187	15.484	0.007	31.2	0.5
100um/40Hz/266nm	SRM612_13	0.0686	0.0020	1.0610	0.0314	15.474	0.006	30.6	0.4
100um/50Hz/266nm	SRM612_14	0.0747	0.0028	1.1549	0.0426	15.460	0.008	29.7	0.5
100um/60Hz/266nm	SRM612_15	0.0578	0.0018	0.8949	0.0281	15.481	0.007	31.0	0.4
100um/60Hz/266nm	SRM612_16	0.0812	0.0044	1.2554	0.0675	15.462	0.007	29.8	0.5
100um/90Hz/266nm	SRM612_17	0.0545	0.0051	0.8440	0.0781	15.501	0.008	32.3	0.5
200um/10Hz/266nm	SRM612_18	0.0159	0.0003	0.2463	0.0054	15.489	0.022	31.5	1.4
200um/20Hz/266nm	SRM612_19	0.0420	0.0006	0.6514	0.0089	15.494	0.005	31.9	0.3
200um/30Hz/266nm	SRM612_20	0.0671	0.0013	1.0376	0.0200	15.472	0.006	30.4	0.4
200um/40Hz/266nm	SRM612_21	0.1066	0.0017	1.6472	0.0256	15.456	0.005	29.4	0.3
200um/40Hz/266nm	SRM612_22	0.1006	0.0023	1.5559	0.0355	15.463	0.006	29.9	0.4
200um/50Hz/266nm	SRM612_23	0.1500	0.0031	2.3132	0.0471	15.423	0.005	27.3	0.3
200um/60Hz/266nm	SRM612_24	0.1737	0.0030	2.6757	0.0459	15.405	0.006	26.1	0.4
200um/90Hz/266nm	SRM612_25	0.2406	0.0073	3.6984	0.1103	15.374	0.007	24.1	0.5

^a: 2SE: 2-standard error

Ablation condition	Sample	¹⁰ B / V	2SE	¹¹ B / V	2SE	¹⁰ B/ ¹¹ B	2SE	δ ¹¹ B	2SE
30um/10Hz/193nm	SRM612_1	0.0109	0.0003	0.0498	0.0014	4.561	0.007	0.8	1.5
30um/20Hz/193nm	SRM612_2	0.0179	0.0006	0.0817	0.0028	4.566	0.005	2.0	1.1
50um/10Hz/193nm	SRM612_3	0.0266	0.0002	0.1212	0.0009	4.560	0.004	0.4	0.8
50um/20Hz/193nm	SRM612_4	0.0483	0.0007	0.2202	0.0033	4.557	0.002	-0.4	0.4
50um/5Hz/193nm	SRM612_5	0.0153	0.0001	0.0700	0.0006	4.565	0.004	1.6	0.9
100um/5Hz/193nm	SRM612_6	0.0448	0.0010	0.2039	0.0047	4.556	0.002	-0.4	0.4
100um/10Hz/193nm	SRM612_7	0.0741	0.0013	0.3369	0.0058	4.549	0.001	-1.6	0.3
100um/1Hz/193nm	SRM612_8	0.0109	0.0001	0.0500	0.0006	4.569	0.006	2.3	1.3
100um/20Hz/193nm	SRM612_9	0.1458	0.0017	0.6620	0.0075	4.541	0.001	-3.8	0.2
100um/2Hz/193nm	SRM612_10	0.0210	0.0001	0.0959	0.0006	4.557	0.003	0.2	0.7
200um/1Hz/193nm	SRM612_11	0.0687	0.0037	0.3139	0.0168	4.571	0.002	2.4	0.5
200um/2Hz/193nm	SRM612_12	0.0835	0.0013	0.3806	0.0059	4.557	0.001	-0.3	0.3
200um/5Hz/193nm	SRM612_13	0.1661	0.0010	0.7543	0.0045	4.542	0.001	-3.5	0.2

^a: 2SE: 2-standard error

Ablation condition	Sample	¹⁰ B	2SE	¹¹ B	2SE	¹⁰ B/ ¹¹ B	2SE	δ ¹¹ B	2SE
30um/10Hz/266nm	SRM612_1	0.0026	0.0001	0.0121	0.0004	4.608	0.026	6.8	5.7
30um/20Hz/266nm	SRM612_2	0.0072	0.0004	0.0328	0.0019	4.579	0.013	0.5	2.9
30um/30Hz/266nm	SRM612_3	0.0081	0.0009	0.0369	0.0043	4.580	0.014	0.7	3.0
50um/10Hz/266nm	SRM612_4	0.0056	0.0001	0.0255	0.0004	4.563	0.016	-3.1	3.5
50um/20Hz/266nm	SRM612_5	0.0142	0.0003	0.0647	0.0014	4.573	0.005	-0.9	1.2
50um/30Hz/266nm	SRM612_6	0.0212	0.0011	0.0969	0.0049	4.571	0.005	-1.3	1.1
50um/40Hz/266nm	SRM612_7	0.0244	0.0018	0.1113	0.0083	4.566	0.004	-2.3	0.8
50um/50Hz/266nm	SRM612_8	0.0264	0.0027	0.1204	0.0122	4.570	0.003	-1.5	0.7
100um/10Hz/266nm	SRM612_9	0.0135	0.0002	0.0621	0.0009	4.589	0.007	2.8	1.5
100um/20Hz/266nm	SRM612_10	0.0317	0.0006	0.1451	0.0029	4.579	0.003	0.4	0.7
100um/30Hz/266nm	SRM612_11	0.0527	0.0011	0.2408	0.0051	4.569	0.002	-1.6	0.4
100um/30Hz/266nm	SRM612_12	0.0522	0.0009	0.2384	0.0042	4.568	0.002	-1.2	0.5
100um/30Hz/266nm	SRM612_13	0.0526	0.0011	0.2400	0.0052	4.565	0.002	-0.8	0.4
100um/40Hz/266nm	SRM612_14	0.0675	0.0020	0.3081	0.0093	4.564	0.002	-2.8	0.3
100um/50Hz/266nm	SRM612_15	0.0791	0.0035	0.3605	0.0161	4.560	0.001	-3.6	0.3
100um/60Hz/266nm	SRM612_16	0.0849	0.0043	0.3868	0.0195	4.559	0.001	-3.8	0.3
100um/70Hz/266nm	SRM612_17	0.0947	0.0057	0.4317	0.0261	4.557	0.001	-4.3	0.3
200um/10Hz/266nm	SRM612_18	0.0191	0.0012	0.0877	0.0054	4.578	0.004	0.2	0.9
200um/20Hz/266nm	SRM612_19	0.0311	0.0009	0.1421	0.0040	4.571	0.003	-1.2	0.7
200um/30Hz/266nm	SRM612_20	0.0731	0.0015	0.3337	0.0070	4.565	0.002	-2.6	0.3
200um/40Hz/266nm	SRM612_21	0.1063	0.0018	0.4846	0.0084	4.558	0.002	-4.2	0.4
200um/50Hz/266nm	SRM612_22	0.1241	0.0021	0.5653	0.0095	4.555	0.001	-4.7	0.2
200um/60Hz/266nm	SRM612_23	0.1320	0.0028	0.6010	0.0129	4.555	0.001	-4.8	0.2
200um/90Hz/266nm	SRM612_24	0.1448	0.0063	0.6591	0.0284	4.551	0.001	-5.6	0.3

^a: 2SE: 2-standard error

ESI Table S2. Analytical results of standard reference materials^a

Sample ID	$\delta^7\text{Li}$	2SE	Sample ID	$\delta^{11}\text{B}$	2SE
BCR-2G(11)_1	2.77	1.93	JB-2(11)_6	7.84	0.49
BCR-2G(11)_2	8.50	1.91	JB-2(11)_7	7.79	0.29
BCR-2G(11)_3	7.70	1.91	JB-2(11)_8	7.69	0.67
BCR-2G(11)_4	5.23	1.66	JB-2(11)_9	7.38	0.46
BCR-2G(11)_5	7.71	1.94	JB-2(11)_10	7.57	0.32
BCR-2G(11-12)_1	3.22	1.31	JB-2(11)_11	7.54	0.65
BCR-2G(11-12)_2	3.40	1.37	JB-2(11)_12	8.42	0.86
BCR-2G(11-12)_3	3.96	1.29	JB-2(11)_13	8.65	0.35
BCR-2G(11-12)_4	4.58	1.21	JB-2(11)_14	9.28	0.88
BCR-2G(11-12)_5	5.61	1.18	JB-2_1	7.95	1.26
BCR-2G(11-12)_6	1.53	1.43	JB-2_2	9.56	1.74
BCR-2G(11-12)_7	0.46	1.30	JB-2_3	7.64	1.11
BCR-2G(11-12)_8	2.78	1.32	JB-2_4	9.27	1.02
BCR-2G(11-12)_9	0.31	1.29	JB-2_5	7.98	1.04
BCR-2G(11-12)_10	3.19	1.32	JB-2(11)_1	4.78	2.86
BCR-2G(11-12)_11	3.03	1.40	JB-2(11)_2	7.73	0.81
BCR-2G(11-12)_12	5.93	1.05	JB-2(11)_3	7.96	0.60
BCR-2G(11-12)_13	3.37	1.15	JB-2(11)_4	8.81	0.48
Average	4.07	4.70	JB-2(11)_5	8.32	0.65
BCR-2G(Ref)	3.48	1.71	JB-2(11)_6	6.87	1.46
			JB-2(11)_7	8.93	1.12
BHVO-2G_1	7.24	2.34	JB-2(11)_8	6.54	0.75
BHVO-2G_2	10.85	2.34	JB-2(11)_9	8.32	0.63
BHVO-2G_3	4.88	1.89	JB-2(11)_10	6.67	0.92
BHVO-2G_4	8.65	2.36	Average	7.90	2.06
BHVO-2G_5	6.08	2.11	JB-2(Ref)	7.24	0.33
Average	7.54	4.64			
BHVO-2G(Ref)	5.90	5.66	BCR-2G(11)_1	-2.09	1.36
			BCR-2G(11)_2	-3.11	2.31
JB-3(11)_1	8.22	2.27	BCR-2G(11)_3	-3.66	2.17
JB-3(11)_2	7.87	1.55	BCR-2G(11)_4	-4.86	2.69
JB-3(11)_3	-1.24	1.04	BCR-2G(11)_5	-3.91	2.99
JB-3(11)_4	-0.66	0.79	BCR-2G(11)_6	-6.06	1.55
JB-3(11)_5	5.63	2.01	BCR-2G(11)_7	-3.70	1.57
Average	3.96	9.20	BCR-2G(11)_8	-3.13	1.71
JB-3(Ref)	3.94	1.00	BCR-2G(11)_9	-2.32	1.15
			BCR-2G(11)_10	-5.45	1.67
GSD-1G_1	33.22	0.61	Average	-3.83	2.58
GSD-1G_2	34.00	0.93	BCR-2G(Ref)	N/A	N/A
GSD-1G_3	33.56	0.74			
GSD-1G_4	34.21	0.71	GSD-1G_1	11.22	0.48
GSD-1G_5	32.90	0.72	GSD-1G_2	9.82	0.48
GSD-1G_3	27.18	0.84	GSD-1G_3	10.28	0.36
GSD-1G_8	27.04	0.65	GSD-1G_4	10.21	0.42
GSD-1G_4	28.63	0.67	GSD-1G_5	9.49	0.44
GSD-1G_5	28.94	0.52	GSD-1G_6	9.04	0.46
GSD-1G_1	27.54	0.55	GSD-1G_7	10.31	0.42
GSD-1G_2	28.21	0.59	GSD-1G_8	10.91	0.34
GSD-1G_3	27.60	0.58	GSD-1G_9	11.53	0.40
GSD-1G_4	26.25	0.66	GSD-1G_10	12.13	0.45
GSD-1G_5	27.18	0.59	Average	10.49	1.91
GSD-1G_6	28.09	0.56	GSD-1G(Ref)	10.27	1.33
GSD-1G_7	28.81	0.52			
GSD-1G_8	27.20	0.54	SRM610(11)_1	-0.19	0.13
GSD-1G_9	27.13	0.67	SRM610(11)_2	-0.29	0.12
GSD-1G_10	26.35	0.63	SRM610(11)_3	-0.22	0.16
Average	29.16	5.64	SRM610(11)_4	-0.41	0.16
GSD-1G(Ref)	30.95	2.26	SRM610(11)_5	-0.52	0.14
			Average	-0.33	0.28
SRM610(11-12)_1	31.88	0.85	SRM610(Ref)	-0.52	0.53
SRM610(11-12)_2	31.20	0.78			
SRM610(11-12)_3	30.97	0.81			
Average	31.35	0.94			
SRM610(Ref)	32.50	1.50			

^a: Ref: reference values from Brand et al. (2014), N/A: not available, 2SE: 2-standard error. Averages are given in 2-standard deviation.

ESI Table S3. Analytical results for GSD-1G using SRM 612 as a standard^a

Run #	Ablation condition	Sample	¹⁰ B / V	2SE	¹¹ B / V	2SE	¹⁰ B/ ¹¹ B	2SE	δ ¹¹ B	2SE
Run1	100um/40Hz/266nm	SRM612_1	0.0536	0.0012	0.2440	0.0053	4.555	0.002		0.4
Run2	100um/40Hz/266nm	GSD-1G_1	0.0716	0.0016	0.3305	0.0072	4.613	0.001	12.0	0.3
Run3	100um/40Hz/266nm	SRM612_2	0.0549	0.0015	0.2500	0.0068	4.556	0.002		0.4
Run4	100um/40Hz/266nm	GSD-1G_2	0.0802	0.0023	0.3698	0.0104	4.612	0.001	11.8	0.2
Run5	100um/40Hz/266nm	SRM612_3	0.0563	0.0019	0.2565	0.0088	4.556	0.002		0.5
Run6	100um/40Hz/266nm	GSD-1G_3	0.0815	0.0024	0.3758	0.0110	4.611	0.001	11.7	0.3
Run7	100um/40Hz/266nm	SRM612_4	0.0561	0.0016	0.2557	0.0073	4.555	0.002		0.4
Run8	100um/40Hz/266nm	GSD-1G_4	0.0721	0.0021	0.3326	0.0098	4.613	0.001	11.9	0.3
Run9	100um/40Hz/266nm	SRM612_5	0.0561	0.0016	0.2558	0.0072	4.557	0.002		0.4
Run10	100um/40Hz/266nm	GSD-1G_5	0.0747	0.0018	0.3446	0.0084	4.614	0.001	12.0	0.3
Run11	100um/40Hz/266nm	SRM612_6	0.0574	0.0018	0.2617	0.0080	4.556	0.001		0.3
Run12	100um/40Hz/266nm	GSD-1G_6	0.0816	0.0024	0.3763	0.0108	4.611	0.001	11.7	0.3
Run13	100um/40Hz/266nm	SRM612_7	0.0580	0.0017	0.2641	0.0077	4.555	0.002		0.4
Run14	100um/40Hz/266nm	GSD-1G_7	0.0805	0.0022	0.3714	0.0099	4.611	0.001	11.8	0.3
Run15	100um/40Hz/266nm	SRM612_8	0.0554	0.0014	0.2522	0.0064	4.556	0.002		0.4
Run16	100um/40Hz/266nm	GSD-1G_8	0.0676	0.0014	0.3119	0.0064	4.614	0.001	12.2	0.3
Run17	100um/40Hz/266nm	SRM612_9	0.0650	0.0023	0.2962	0.0105	4.556	0.002		0.3
Run18	100um/40Hz/266nm	GSD-1G_9	0.0682	0.0018	0.3144	0.0083	4.612	0.002	11.8	0.4
Run19	100um/40Hz/266nm	SRM612_10	0.0585	0.0014	0.2666	0.0063	4.557	0.002		0.4
Run20	100um/40Hz/266nm	GSD-1G_10	0.0811	0.0023	0.3741	0.0106	4.614	0.001	11.9	0.3
Run21	100um/40Hz/266nm	SRM612_11	0.0595	0.0015	0.2714	0.0069	4.558	0.002		0.3
Run22	100um/40Hz/266nm	GSD-1G_11	0.0885	0.0010	0.4080	0.0047	4.613	0.001	11.7	0.3
Run23	100um/40Hz/266nm	SRM612_12	0.0622	0.0015	0.2835	0.0066	4.557	0.002		0.4
Run24	100um/40Hz/266nm	GSD-1G_12	0.0893	0.0012	0.4119	0.0055	4.613	0.001	11.6	0.2
Run25	100um/40Hz/266nm	SRM612_13	0.0592	0.0014	0.2697	0.0065	4.558	0.002		0.3
Run26	100um/40Hz/266nm	GSD-1G_13	0.0868	0.0012	0.4005	0.0057	4.613	0.001	11.6	0.2
Run27	100um/40Hz/266nm	SRM612_14	0.0607	0.0014	0.2765	0.0064	4.557	0.002		0.3
Run28	100um/40Hz/266nm	GSD-1G_14	0.0862	0.0013	0.3972	0.0059	4.610	0.001	11.3	0.3
Run29	100um/40Hz/266nm	SRM612_15	0.0657	0.0019	0.2995	0.0084	4.556	0.002		0.4
Run30	100um/40Hz/266nm	GSD-1G_15	0.0879	0.0012	0.4050	0.0055	4.609	0.001	11.2	0.2
Run31	100um/40Hz/266nm	SRM612_16	0.0612	0.0014	0.2790	0.0065	4.556	0.002		0.4
Run32	100um/40Hz/266nm	GSD-1G_16	0.0875	0.0008	0.4034	0.0035	4.609	0.001	10.8	0.3
Run33	100um/40Hz/266nm	SRM612_17	0.0619	0.0018	0.2822	0.0083	4.559	0.002		0.4
Run34	100um/40Hz/266nm	GSD-1G_17	0.0869	0.0009	0.4004	0.0040	4.609	0.001	10.6	0.3
Run35	100um/40Hz/266nm	SRM612_18	0.0628	0.0015	0.2862	0.0068	4.557	0.001		0.3
Run36	100um/40Hz/266nm	GSD-1G_18	0.0881	0.0007	0.4057	0.0034	4.608	0.001	10.5	0.2
Run37	100um/40Hz/266nm	SRM612_19	0.0607	0.0015	0.2764	0.0067	4.557	0.002		0.4
Run38	100um/40Hz/266nm	GSD-1G_19	0.0862	0.0009	0.3976	0.0043	4.609	0.001	10.8	0.3
Run39	100um/40Hz/266nm	SRM612_20	0.0599	0.0012	0.2730	0.0054	4.559	0.002		0.4
Run40	100um/40Hz/266nm	GSD-1G_20	0.0851	0.0008	0.3924	0.0035	4.611	0.001	11.1	0.3
Run41	100um/40Hz/266nm	SRM612_21	0.0589	0.0012	0.2687	0.0057	4.558	0.002		0.3

^a: 2SE: 2-standard error

ESI Table S4. Analytical results for SRM 612 with reference to ablation crater volume^a

Run #	Ablation condition	Sample	⁶ Li / V	2SE	⁷ Li / V	2SE	⁷ Li/ ⁶ Li	2SE	δ ⁷ Li	2SE	Volume	Depth
Run2	100um/1Hz/193nm (130 mJ)	SRM612_2	0.0124	0.0007	0.1890	0.0101	15.225	0.025	30.8	1.6	50127	10
Run3	100um/3Hz/193nm (130 mJ)	SRM612_3	0.0331	0.0009	0.5040	0.0140	15.244	0.011	32.0	0.7	135799	28
Run4	100um/5Hz/193nm (130 mJ)	SRM612_4	0.0481	0.0018	0.7332	0.0266	15.232	0.011	31.2	0.7	218730	45
Run5	100um/7Hz/193nm (130 mJ)	SRM612_5	0.0640	0.0015	0.9747	0.0233	15.231	0.008	31.1	0.5	284782	59
Run6	100um/10Hz/193nm (130 mJ)	SRM612_6	0.0915	0.0021	1.3913	0.0323	15.212	0.006	29.9	0.4	345468	75
Run7	100um/15Hz/193nm (130 mJ)	SRM612_7	0.1360	0.0030	2.0633	0.0451	15.174	0.004	27.4	0.3	441026	100
Run8	100um/20Hz/193nm (130 mJ)	SRM612_8	0.1743	0.0050	2.6397	#NAME?	15.147	0.005	25.6	0.3	550619	130
Run10	100um/1Hz/193nm (130 mJ)	SRM612_10	0.0131	0.0006	0.1999	0.0086	15.208	0.026	30.4	1.7	50127	10
Run11	100um/3Hz/193nm (130 mJ)	SRM612_11	0.0346	0.0010	0.5260	0.0158	15.204	0.010	30.1	0.7	135799	28
Run12	100um/5Hz/193nm (130 mJ)	SRM612_12	0.0534	0.0014	0.8125	0.0213	15.220	0.009	31.2	0.6	218730	45
Run13	100um/7Hz/193nm (130 mJ)	SRM612_13	0.0735	0.0019	1.1182	0.0294	15.222	0.009	31.3	0.6	284782	59
Run14	100um/10Hz/193nm (130 mJ)	SRM612_14	0.1045	0.0025	1.5877	0.0388	15.191	0.005	29.3	0.3	345468	75
Run15	100um/15Hz/193nm (130 mJ)	SRM612_15	0.1468	0.0038	2.2267	0.0571	15.164	0.004	27.5	0.3	441026	100
Run16	100um/20Hz/193nm (130 mJ)	SRM612_16	0.1797	0.0038	2.7207	0.0571	15.141	0.005	26.0	0.3	550619	130
Run #	Ablation condition	Sample	¹⁰ B / V	2SE	¹¹ B / V	2SE	¹⁰ B/ ¹¹ B	2SE	δ ¹¹ B	2SE	Volume	Depth
Run2	100um/1Hz/193nm (130 mJ)	SRM612_2	0.0086	0.0004	0.0388	0.0018	4.531	0.009	1.1	2.0	50127	10
Run3	100um/3Hz/193nm (130 mJ)	SRM612_3	0.0228	0.0009	0.1032	0.0039	4.525	0.004	-0.3	0.9	135799	28
Run4	100um/5Hz/193nm (130 mJ)	SRM612_4	0.0361	0.0015	0.1634	0.0067	4.524	0.002	-0.5	0.5	218730	45
Run5	100um/7Hz/193nm (130 mJ)	SRM612_5	0.0486	0.0018	0.2197	0.0080	4.525	0.002	-0.2	0.4	284782	59
Run6	100um/10Hz/193nm (130 mJ)	SRM612_6	0.0672	0.0017	0.3036	0.0077	4.521	0.001	-1.2	0.3	345468	75
Run7	100um/15Hz/193nm (130 mJ)	SRM612_7	0.0937	0.0020	0.4232	0.0090	4.517	0.001	-2.2	0.3	441026	100
Run8	100um/20Hz/193nm (130 mJ)	SRM612_8	0.1132	0.0033	0.5107	0.0150	4.513	0.001	-3.0	0.3	550619	130
Run10	100um/1Hz/193nm (130 mJ)	SRM612_10	0.0085	0.0004	0.0385	0.0019	4.530	0.009	0.5	2.0	50127	10
Run11	100um/3Hz/193nm (130 mJ)	SRM612_11	0.0227	0.0007	0.1027	0.0032	4.530	0.003	0.5	0.7	135799	28
Run12	100um/5Hz/193nm (130 mJ)	SRM612_12	0.0359	0.0014	0.1623	0.0064	4.525	0.003	-0.5	0.6	218730	45
Run13	100um/7Hz/193nm (130 mJ)	SRM612_13	0.0473	0.0014	0.2141	0.0065	4.524	0.002	-0.7	0.4	284782	59
Run14	100um/10Hz/193nm (130 mJ)	SRM612_14	0.0639	0.0015	0.2891	0.0068	4.523	0.001	-1.0	0.3	345468	75
Run15	100um/15Hz/193nm (130 mJ)	SRM612_15	0.0917	0.0022	0.4144	0.0101	4.519	0.001	-1.9	0.3	441026	100
Run16	100um/20Hz/193nm (130 mJ)	SRM612_16	0.1148	0.0030	0.5183	0.0133	4.515	0.001	-2.7	0.3	550619	130

^a: 2SE: 2-standard error, volume: μm³, depth μm

ESI Table S5. Analytical results for jadeite using crater volume-corrected LA-MFC-ICPMS^a

Run #	Ablation condition	Sample	Crat. vol. (µm ³)	Li (ppm)	2SE (ppm)	⁶ Li / V	2SE	⁷ Li / V	2SE	⁷ Li/ ⁶ Li	2SE	δ ⁷ Li	δ ⁷ Li (vcv)	2SE
Run1	100um/10Hz/193nm (150 mJ)	SRM612_1	549779	40.2		0.0930	0.0026	1.4654	0.0405	15.750	0.010	31.20		0.65
Run2	100um/10Hz/193nm (150 mJ)	Jade-0	290597	20.2	0.9	0.0261	0.0012	0.3981	0.0180	15.276	0.018	1.00	0.65	1.15
Run3	100um/10Hz/193nm (150 mJ)	SRM612_2	549779			0.0976	0.0021	1.5369	0.0335	15.753	0.014			0.86
Run4	100um/10Hz/193nm (150 mJ)	Jade-1	290597	28.3	0.7	0.0373	0.0009	0.5690	0.0133	15.271	0.010	0.05	-0.30	0.62
Run5	100um/10Hz/193nm (150 mJ)	SRM612_3	549779			0.0968	0.0025	1.5262	0.0393	15.770	0.009			0.58
Run6	100um/10Hz/193nm (150 mJ)	Jade-2	290597	39.4	1.6	0.0515	0.0021	0.7848	0.0314	15.251	0.010	-0.76	-1.11	0.64
Run7	100um/10Hz/193nm (150 mJ)	SRM612_4	549779			0.0954	0.0019	1.5021	0.0307	15.738	0.010			0.66
Run8	100um/10Hz/193nm (150 mJ)	Jade-3	290597	21.6	1.0	0.0286	0.0013	0.4355	0.0202	15.226	0.012	-0.63	-0.98	0.82
Run9	100um/10Hz/193nm (150 mJ)	SRM612_5	549779			0.0996	0.0011	1.5651	0.0174	15.715	0.011			0.70
Run10	100um/10Hz/193nm (150 mJ)	Jade-4	290597	10.4	0.4	0.0140	0.0005	0.2125	0.0075	15.153	0.019	-5.53	-5.88	1.27
Run11	100um/10Hz/193nm (150 mJ)	SRM612_6	549779			0.0972	0.0009	1.5305	0.0138	15.746	0.010			0.65
Run12	100um/10Hz/193nm (150 mJ)	Jade-5	290597	11.2	0.4	0.0148	0.0006	0.2237	0.0088	15.134	0.019	-8.35	-8.70	1.27
Run13	100um/10Hz/193nm (150 mJ)	SRM612_7	549779			0.0950	0.0008	1.4980	0.0132	15.769	0.011			0.68
Run14	100um/10Hz/193nm (150 mJ)	Jade-6	290597	21.0	0.9	0.0264	0.0011	0.4030	0.0177	15.252	0.017	-1.88	-2.23	1.09
Run15	100um/10Hz/193nm (150 mJ)	SRM612_8	549779			0.0900	0.0009	1.4205	0.0144	15.779	0.012			0.74
Run16	100um/10Hz/193nm (150 mJ)	Jade-7	290597	9.3	0.4	0.0114	0.0004	0.1721	0.0067	15.132	0.031	-9.57	-9.92	2.02
Run17	100um/10Hz/193nm (150 mJ)	SRM612_9	549779			0.0892	0.0009	1.4068	0.0146	15.772	0.010			0.64
Run18	100um/10Hz/193nm (150 mJ)	Jade-8	290597	16.2	0.9	0.0196	0.0010	0.2978	0.0159	15.213	0.020	-4.05	-4.40	1.29
Run19	100um/10Hz/193nm (150 mJ)	SRM612_10	549779			0.0883	0.0011	1.3918	0.0169	15.766	0.010			0.61
Run20	100um/10Hz/193nm (150 mJ)	Jade-9	290597	17.3	0.8	0.0208	0.0009	0.3162	0.0145	15.209	0.019	-4.09	-4.44	1.25
Run21	100um/10Hz/193nm (150 mJ)	SRM612_11	549779			0.0885	0.0008	1.3953	0.0135	15.765	0.008			0.52
Run22	100um/10Hz/193nm (150 mJ)	Jade-10	290597	10.9	0.7	0.0136	0.0008	0.2060	0.0123	15.182	0.028	-4.69	-5.04	1.84
Run23	100um/10Hz/193nm (150 mJ)	SRM612_12	549779			0.0934	0.0014	1.4685	0.0230	15.728	0.011			0.68
Run24	100um/10Hz/193nm (150 mJ)	Jade-11	290597	11.4	0.7	0.0145	0.0009	0.2206	0.0136	15.164	0.029	-5.28	-5.63	1.90
Run25	100um/10Hz/193nm (150 mJ)	SRM612_13	549779			0.0937	0.0015	1.4759	0.0232	15.749	0.007			0.46
Run26	100um/10Hz/193nm (150 mJ)	Jade-12	290597	13.5	0.4	0.0173	0.0006	0.2624	0.0085	15.209	0.019	-2.84	-3.19	1.25
Run27	100um/10Hz/193nm (150 mJ)	SRM612_14	549779			0.0947	0.0015	1.4904	0.0238	15.742	0.012			0.79
Run28	100um/10Hz/193nm (150 mJ)	Jade-13	290597	12.5	0.6	0.0159	0.0008	0.2415	0.0124	15.183	0.022	-3.76	-4.11	1.43
Run29	100um/10Hz/193nm (150 mJ)	SRM612_15	549779			0.0916	0.0018	1.4408	0.0280	15.723	0.010			0.62
Run30	100um/10Hz/193nm (150 mJ)	Jade-14	290597	12.5	0.4	0.0162	0.0005	0.2443	0.0074	15.121	0.017	-7.35	-7.70	1.10
Run31	100um/10Hz/193nm (150 mJ)	SRM612_16	549779			0.0982	0.0022	1.5441	0.0341	15.731	0.007			0.44
Average / 1SD				17.0	8.2					Average / 2SD			-4.2	6.2
Run #	Ablation condition	Sample	Crat. vol. (µm ³)	Li (ppm)	2SE (ppm)	⁶ Li / V	2SE	⁷ Li / V	2SE	⁷ Li/ ⁶ Li	2SE	δ ⁷ Li		2SE
Run31	100um/10Hz/193nm (150 mJ)	SRM612_16	549779	40.2		0.0982	0.0022	1.5441	0.0341	15.731	0.007	31.20		0.44
Run32	100um/5Hz/193nm (150 mJ)	SRM612_17	314159	39.5	1.1	0.0552	0.0016	0.8679	0.0247	15.726	0.009	30.88		0.55
Run31	100um/10Hz/193nm (150 mJ)	SRM612_16	549779			0.0982	0.0022	1.5441	0.0341	15.731	0.007			0.44
Run34	100um/15Hz/193nm (150 mJ)	SRM612_18	785398	39.7	0.9	0.1384	0.0030	2.1759	0.0481	15.718	0.009	30.41		0.60
Run31	100um/10Hz/193nm (150 mJ)	SRM612_16	549779			0.0982	0.0022	1.5441	0.0341	15.731	0.007			0.44
Run36	100um/20Hz/193nm (150 mJ)	SRM612_19	1044580	37.8	0.7	0.1756	0.0031	2.7576	0.0486	15.705	0.008	29.57		0.52
Run31	100um/10Hz/193nm (150 mJ)	SRM612_16	549779			0.0982	0.0022	1.5441	0.0341	15.731	0.007			0.44

^a: 2SE: 2-standard error, volume: µm³, depth µm; Crat. Vol.: crater volume; vcv: volume-corrected value. Run 31 to 36 were used for crater volume correction calculations

ESI Table S6. Analytical results for tourmaline using crater volume-corrected LA-MFC-ICPMS^a

Run #	Ablation condition	Sample	Crat. vol. (μm^3)	B (ppm)	2SE (ppm)	$^{10}\text{B}/\text{V}$	2SE	$^{11}\text{B}/\text{V}$	2SE	$^{10}\text{B}/^{11}\text{B}$	2SE	$\delta^{11}\text{B}$	$\delta^{11}\text{B}$ (vcv)	2SE
Run1	50um/3Hz/193nm (130 ml)	SRM610_1	56941	350		0.0622	0.0011	0.2859	0.0051	4.5973	0.0016	-0.01		0.34
Run2	50um/3Hz/193nm (130 ml)	Tourm-1	25525	27796	2207	2.2527	0.1787	10.2750	0.8160	4.5609	0.0005	-8.26	-8.36	0.11
Run3	50um/3Hz/193nm (130 ml)	SRM610_2	56941			0.0633	0.0011	0.2914	0.0054	4.6003	0.0019			0.41
Run4	50um/3Hz/193nm (130 ml)	Tourm-2	25525	29641	1521	2.4636	0.1263	11.2422	0.5769	4.5631	0.0005	-8.06	-8.16	0.10
Run5	50um/3Hz/193nm (130 ml)	SRM610_3	56941			0.0654	0.0011	0.3010	0.0048	4.6000	0.0015			0.33
Run6	50um/3Hz/193nm (130 ml)	Tourm-3	25525	28888	1334	2.4461	0.1129	11.1657	0.5158	4.5646	0.0004	-7.87	-7.97	0.09
Run7	50um/3Hz/193nm (130 ml)	SRM610_4	56941			0.0657	0.0012	0.3025	0.0053	4.6015	0.0017			0.36
Run8	50um/3Hz/193nm (130 ml)	Tourm-4	25525	25386	1859	2.1563	0.1577	9.8425	0.7206	4.5642	0.0005	-8.11	-8.21	0.11
Run9	50um/3Hz/193nm (130 ml)	SRM610_5	56941			0.0658	0.0010	0.3029	0.0047	4.6015	0.0016			0.35
Run10	50um/3Hz/193nm (130 ml)	Tourm-5	25525	24170	1882	2.0146	0.1567	9.1938	0.7160	4.5630	0.0007	-8.38	-8.48	0.16
Run11	50um/3Hz/193nm (130 ml)	SRM610_6	56941			0.0633	0.0009	0.2913	0.0039	4.6016	0.0013			0.28
Run12	50um/3Hz/193nm (130 ml)	Tourm-6	25525	25263	1787	2.0601	0.1455	9.4036	0.6652	4.5640	0.0008	-8.42	-8.52	0.17
Run13	50um/3Hz/193nm (130 ml)	SRM610_7	56941			0.0630	0.0008	0.2899	0.0036	4.6038	0.0017			0.37
Run14	50um/3Hz/193nm (130 ml)	Tourm-7	25525	24622	1878	2.0033	0.1525	9.1459	0.6977	4.5647	0.0009	-8.45	-8.55	0.19
Run15	50um/3Hz/193nm (130 ml)	SRM610_8	56941			0.0630	0.0009	0.2901	0.0041	4.6033	0.0016			0.35
Run16	50um/3Hz/193nm (130 ml)	Tourm-8	25525	23603	1900	1.9403	0.1561	8.8583	0.7131	4.5650	0.0006	-8.36	-8.46	0.12
Run17	50um/3Hz/193nm (130 ml)	SRM610_9	56941			0.0643	0.0005	0.2960	0.0023	4.6037	0.0015			0.32
Run18	50um/3Hz/193nm (130 ml)	Tourm-9	25525	23068	1947	1.9203	0.1619	8.7668	0.7399	4.5650	0.0006	-8.25	-8.35	0.14
Run19	50um/3Hz/193nm (130 ml)	SRM610_10	56941			0.0646	0.0007	0.2974	0.0033	4.6021	0.0015			0.33
Run20	50um/3Hz/193nm (130 ml)	Tourm-10	25525	22777	1843	1.8986	0.1535	8.6679	0.7012	4.5652	0.0005	-8.41	-8.51	0.12
Run21	50um/3Hz/193nm (130 ml)	SRM610_11	56941			0.0644	0.0006	0.2968	0.0027	4.6056	0.0014			0.31
Run22	50um/3Hz/193nm (130 ml)	Tourm-11	25525	23833	2037	1.9724	0.1684	9.0053	0.7698	4.5651	0.0007	-8.80	-8.90	0.15
Run23	50um/3Hz/193nm (130 ml)	SRM610_12	56941			0.0637	0.0007	0.2932	0.0033	4.6057	0.0014			0.30
Run24	50um/3Hz/193nm (130 ml)	Tourm-12	25525	24407	2109	1.9964	0.1723	9.1145	0.7874	4.5651	0.0006	-8.64	-8.74	0.13
Run25	50um/3Hz/193nm (130 ml)	SRM610_13	56941			0.0630	0.0009	0.2899	0.0039	4.6040	0.0016			0.36
Run26	50um/3Hz/193nm (130 ml)	Tourm-13	25525	24522	1937	1.9894	0.1570	9.0893	0.7180	4.5684	0.0005	-7.82	-7.92	0.12
Run27	50um/3Hz/193nm (130 ml)	SRM610_14	56941			0.0627	0.0005	0.2889	0.0025	4.6047	0.0015			0.32
Run28	50um/3Hz/193nm (130 ml)	Tourm-14	25525	25755	2023	2.0804	0.1633	9.5012	0.7464	4.5665	0.0006	-8.29	-8.39	0.14
Run29	50um/3Hz/193nm (130 ml)	SRM610_15	56941			0.0624	0.0006	0.2872	0.0027	4.6045	0.0015			0.33
Run30	50um/3Hz/193nm (130 ml)	Tourm-15	25525	27171	1932	2.1528	0.1529	9.8324	0.6990	4.5671	0.0005	-8.13	-8.23	0.11
Run31	50um/3Hz/193nm (130 ml)	SRM610_16	56941			0.0604	0.0007	0.2780	0.0032	4.6044	0.0020			0.42
		Average / 1SD		25394	2088					Average / 2SD			-8.4	0.5
Run #	Ablation condition	Sample	Crat. vol. (μm^3)	B (ppm)	2SE (ppm)	$^{10}\text{B}/\text{V}$	2SE	$^{11}\text{B}/\text{V}$	2SE	$^{10}\text{B}/^{11}\text{B}$	2SE	$\delta^{11}\text{B}$	$\delta^{11}\text{B}$ (vcv)	2SE
Run31	50um/3Hz/193nm (130 ml)	SRM610_16	56941			0.0604	0.0007	0.2780	0.0032	4.6044	0.0020	-0.01		0.42
Run32	50um/1Hz/193nm (130 ml)	SRM610_C1	20597	350	20	0.0218	0.0013	0.1006	0.0058	4.6031	0.0042	-0.30	-0.50	0.90
Run31	50um/3Hz/193nm (130 ml)	SRM610_16	56941			0.0604	0.0007	0.2780	0.0032	4.6044	0.0020			0.42
Run33	50um/2Hz/193nm (130 ml)	SRM610_C2	40346	350	6	0.0428	0.0007	0.1970	0.0032	4.6049	0.0022	0.09	-0.11	0.48
Run31	50um/3Hz/193nm (130 ml)	SRM610_16	56941			0.0604	0.0007	0.2780	0.0032	4.6044	0.0020			0.42
Run34	50um/5Hz/193nm (130 ml)	SRM610_C3	89981	350	5	0.0954	0.0013	0.4393	0.0058	4.6067	0.0012	0.48	0.28	0.25
Run31	50um/3Hz/193nm (130 ml)	SRM610_16	56941			0.0604	0.0007	0.2780	0.0032	4.6044	0.0020			0.42
Run35	50um/7Hz/193nm (130 ml)	SRM610_C4	123649	350	5	0.1311	0.0018	0.6037	0.0081	4.6063	0.0009	0.40	0.20	0.20
Run31	50um/3Hz/193nm (130 ml)	SRM610_16	56941			0.0604	0.0007	0.2780	0.0032	4.6044	0.0020			0.42
Run36	50um/10Hz/193nm (130 ml)	SRM610_C5	168105	350	4	0.1782	0.0022	0.8208	0.0099	4.6068	0.0007	0.50	0.30	0.15
Run31	50um/3Hz/193nm (130 ml)	SRM610_16	56941			0.0604	0.0007	0.2780	0.0032	4.6044	0.0020			0.42
Run37	50um/15Hz/193nm (130 ml)	SRM610_C6	233222	350	7	0.2471	0.0048	1.1387	0.0221	4.6077	0.0009	0.69	0.49	0.19
Run31	50um/3Hz/193nm (130 ml)	SRM610_16	56941			0.0604	0.0007	0.2780	0.0032	4.6044	0.0020			0.42
Run38	50um/20Hz/193nm (130 ml)	SRM610_C7	299471	350	8	0.3173	0.0073	1.4621	0.0333	4.6079	0.0008	0.76	0.56	0.17
Run31	50um/3Hz/193nm (130 ml)	SRM610_16	56941			0.0604	0.0007	0.2780	0.0032	4.6044	0.0020			0.42
Run39	100um/10Hz/193nm (130 ml)	SRM610_C8	591412	350	5	0.6275	0.0087	2.8875	0.0403	4.6016	0.0004	-0.61	-0.81	0.08
Run31	50um/3Hz/193nm (130 ml)	SRM610_16	56941			0.0604	0.0007	0.2780	0.0032	4.6044	0.0020			0.42
Run40	100um/5Hz/193nm (130 ml)	SRM610_C9	337282	350	2	0.3577	0.0020	1.6467	0.0090	4.6033	0.0004	-0.26	-0.46	0.10
Run31	50um/3Hz/193nm (130 ml)	SRM610_16	56941			0.0604	0.0007	0.2780	0.0032	4.6044	0.0020			0.42
Run50	100um/3Hz/193nm (130 ml)	SRM610_C10	216420	350	3	0.2295	0.0019	1.0566	0.0089	4.6037	0.0006	-0.16	-0.36	0.12
Run31	50um/3Hz/193nm (130 ml)	SRM610_16	56941			0.0604	0.0007	0.2780	0.0032	4.6044	0.0020			0.42
Run52	100um/1Hz/193nm (130 ml)	SRM610_C11	83377	350	8	0.0884	0.0020	0.4071	0.0094	4.6057	0.0014	0.26	0.06	0.31
Run31	50um/3Hz/193nm (130 ml)	SRM610_16	56941			0.0604	0.0007	0.2780	0.0032	4.6044	0.0020			0.42

^a: 2SE: 2-standard error, volume: μm^3 , depth μm ; Crat. Vol.: crater volume; vcv: volume-corrected value. Run 31 to 36 were used for crater volume correction calculations